THE EFFECT OF ATMOSPHERIC GASES ON THE ELECTRICAL STABILITY OF GRAPHENE

A Thesis Submitted to
the Graduate School of Engineering and Sciences of
İzmir Institute of Technology
in Partial Fulfillment of the Requirements for the Degree of

MASTER OF SCIENCE

in Physics

by
Sırrı Batuhan KALKAN

December 2017
İZMİR

We approve the thesis of **Sırrı Batuhan KALKAN**

Examining Committee Members:

Assoc. Prof. Dr. Cem ÇELEBİ
Department of Physics, İzmir Institute of Technology

Assoc. Prof. Dr. Hasan ŞAHİN
Department of Photonics, İzmir Institute of Technology

Assist. Prof. Dr. Özhan ÜNVERDİ
Department of Electric Electronic Engineering, Yaşar University

20 December 2017

Assoc. Prof. Dr. Cem ÇELEBİ
Supervisor, Department of Physics
İzmir Institute of Technology

Prof. Dr. Ramazan Tuğrul SENGER
Head of the Department of Physics

Prof. Dr. Aysun SOFUOĞLU
Dean of the Graduate School of
Engineering and Sciences

ACKNOWLEDGEMENTS

It is my pleasure to acknowledge and express my gratitude those who helped me along the way to completion of this thesis.

I would like to thank my supervisor Assoc. Prof. Dr. Cem Çelebi for his invaluable advices, encouragement and for all brainstorming that we conduct throughout this study.

I am thankful for the committee members of my thesis Assoc. Prof. Dr. Hasan Şahin and Assist. Prof. Dr. Özhan Ünverdi for their participations and proofreading's. I am also grateful to Assoc. Prof. Dr. Afif Sıddıki for his guidance and favor.

I also would like to thank my lab mates Erdi Kuşdemir, Dilce Özkendir, Hasan Aydın and all the members of Quantum Device Laboratory for their support, discuss and patience for my thrill.

I am also thankful to my cycling team Flamme Rouge İzmir and the special members of the club. And also, the valuable members of IZTECH Road Cycling.

I am also grateful to my squad members Gökhan Öztarhan, Barış Akbalı and Korhan E. Çakmak for their friendship and entertaining moments.

I wish like to thank to my love, Hande Yurdatapan, who is always at my side how long or how hard does it takes.

And last but not least, I am also thankful to my family for their endless support and for especially my mother who is always ready to pick me up after all the calamities.

ABSTRACT

THE EFFECT OF ATMOSPHERIC GASES ON THE ELECTRICAL STABILITY OF GRAPHENE

In this thesis, adsorbate induced variations in the electrical conductivity of graphene layers with two different types of charge carriers are investigated experimentally by using Transient Photocurrent Spectroscopy (TPS) method. In-vacuum TPS measurements taken for a duration of *5 ks*, revealed that the adsorption/desorption of atmospheric adsorbates leads to a 45 % increment and 110 % decrement in the conductivity of CVD graphene (p--type) and epitaxial graphene (n-type) layers on semi-insulation (SI) Silicon Carbide (SiC) substrates, respectively. The graphene layers on SI-SiC substrates are encapsulated and passivated with thin SiO_2 film grown by Thermal Evaporation and Pulsed Electron Deposition (PED) techniques. The measurements conducted for short periods and a few cycles showed that the thermal passivation of graphene layers is insufficient. However, the PED encapsulation process completely suppresses the time-dependent conductivity instability of graphene independent of its charge carrier type. The obtained results are used to construct an experimental model for identifying adsorbate related conductivity variations in graphene and also in other 2D materials with inherently high surface-to-volume ratio.

ÖZET

ATMOSFERİK GAZLARIN GRAFENİN ELEKTRİKSEL KARARLILIĞI ÜZERİNDEKİ ETKİSİ

Bu çalışmada, iki farklı yük taşıyıcı türüne sahip grafen katmanlarının adsorbant dolaylı elektriksel iletkenlik değişimleri deneysel olarak zamana bağlı fotoakım spektroskopisi metoduyla incelenmiştir. Vakumda yapılan *5 ks* periyotlu spektroskopi ölçümleri atmosferik adsorbantların yüzeye tutunmalarının/yüzeyden salınmalarının, yarı-yalıtkan silikon karbür alttaşları üzerindeki CVD grafen (p-tipi) için 45 % iletkenlik artışına, epitaksiyel grafen (n-tipi) için 110 % iletkenlik azalışına sebep olduğu ortaya çıkarılmıştır. Yarı-yalıtkan silikon karbür üzerindeki grafen katmanları Termal Buharlaştırma ve Atımlı Elektron Kaplama teknikleriyle büyütülen SiO_2 ince filmleriyle enkapsüle ve pasive edilmiştir. Kısa periyotlarla ve birkaç döngülü olarak yürütülen ölçümlerde, grafen katmanlarının termal metotlarla pasivasyonunun yetersiz olduğunu gözlemlenmiştir. Bununla birlikte, AEK enkapsülasyon işleminin grafendeki zamana bağlı iletkenlik kararsızlıklarının grafenin taşıyıcı yoğunluğundan bağımsız olmak üzere tamamen bastırıldığını göstermiştir. Elde edilen sonuçlar grafende ve kendiliğinden yüzey alanının hacme oranının oldukça yüksek olduğu diğer iki boyutlu malzemelerde adsorbant dolaylı iletkenlik değişimlerine deneysel bir model kurulmasına olanak sağlamıştır.

TABLE OF CONTENTS

LIST OF FIGURES

Figure **Page**

LIST OF TABLES

LIST OF ABBREVIATIONS

2D . . . . . Two Dimensional
UV . . . . . UltraViolet
CVD . . . . . Chemical Vapor Deposition
NIR . . . . . Near Infra Red
TCE . . . . . Transparent Conductive Electrode
ITO . . . . . Indium Tin Oxide
MSM . . . . . Metal-Semiconductor-Metal
MS . . . . . Metal-Semiconductor
TPS . . . . . Transient Photocurrent Spectroscopy
PED . . . . . Pulsed Electron Deposition
TE . . . . . Thermal Evaporation
GFET . . . . . Graphene Field Effect Transistor
SLG . . . . . Single Layer Graphene
SI . . . . . Semi-Insulating
UHV . . . . . Ultra High Vacuum
TMP . . . . . Turbo Molecular Pump
MEG . . . . . Monolayer Epitaxial Graphene
W . . . . . Tungsten
FWHM . . . . . Full Width at Half Maximum
CVDG . . . . . Chemical Vapor Deposited Graphene
EG . . . . . Epitaxial Graphene
B-CVDG . . . . . Bare Chemical Vapor Deposited Graphene
B-EG . . . . . Bare Epitaxial Graphene
TE-CVDG . . . . . Thermally Encapsulated Chemical Vapor Deposited Graphene
TE-EG . . . . . Thermally Encapsulated Epitaxial Graphene
PED-CVDG . . . . . PED Encapsulated Chemical Vapor Deposited Graphene
PED-EG . . . . . PED Encapsulated Epitaxial Graphene

CHAPTER 1

INTRODUCTION

1.1. Graphene and It's Importance

Different from their bulk counterparts, layered materials exhibit novel properties when they are thinned to their physical limits. These materials are called 2D materials. Graphene is the rising star of many researches owing to its extraordinary electronic and mechanical properties like being one atom thick and zero bandgap semiconductor (Geim et al. (2007), Cooper et al. (2012)). Graphene is composed of sp^2 hybridized carbon atoms allocated in a honeycomb lattice. By means of electronic properties, the significance of graphene rises from the Dirac cone of its dispersion diagram, which leads to electrons acting as massless particles. In this manner, one could assume that the mobility of the electrons in the graphene lattice, thus the conductivity of this 2D material should be infinite. However when the scattering mechanisms, such as phonon scattering, defects in the lattice structure and the substrate effects limit the mobility in graphene films. Bolotin et al. (2008) experimentally showed that a mobility of more than $200.000\ cm^2/V.s$ can be obtained in suspended graphene at $4.2\ K$. High carrier mobility and high conductivity are the two crucial points for researchers when designing electronic devices. In this manner, a graphene based device is expected to outperform to the one devices based on silicon technology. Apart from its exceptional electronic properties, Bonaccorso et al. (2010) showed that graphene exhibits high optical transparency in the ultraviolet (UV) and visible spectrum, which places this material as the topmost choice to be integrated as transparent conductive electrode.

1.2. Morphological Structure of Graphene

The carbon atoms in the graphene lattice have sp^2 hybridization. The in-plane sigma (σ) bonds, known as s, p_x and p_y, are exceptionally strong; thus they yield to a stable hexagonal structure. p_z orbitals are partially filled and are responsible for the

conduction of the electrons. Between the graphene sheets, sp^3 hybridization is observed, the out of plane π-orbitals induces weak van der Waals forces.

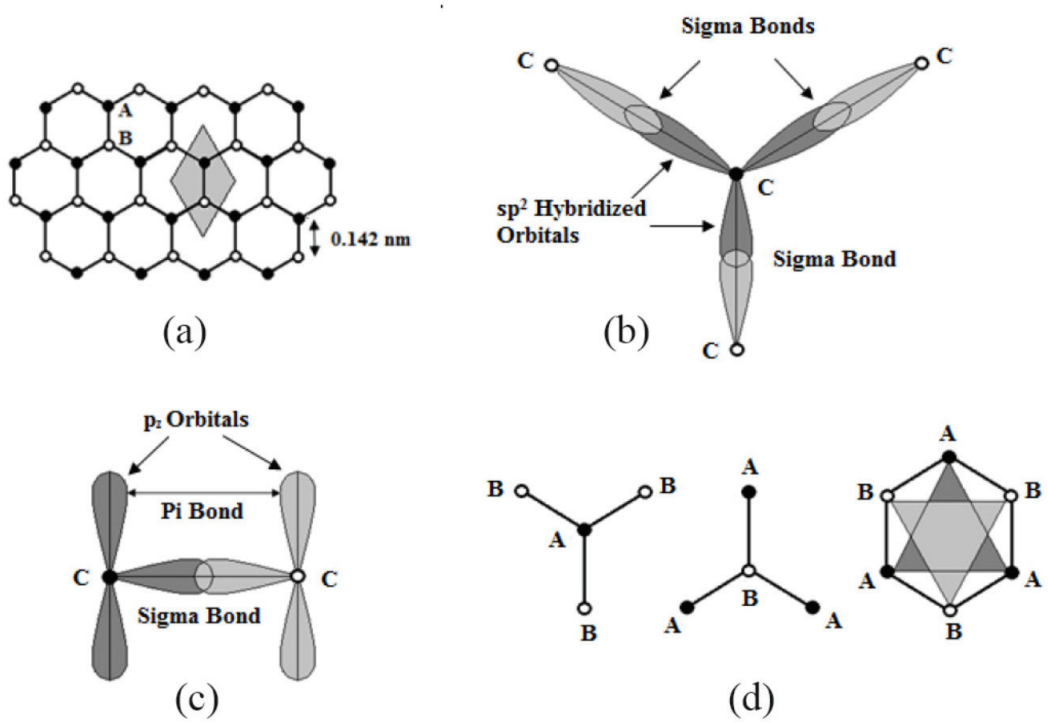

Figure 1.1. (a) Honeycomb lattice of carbon atoms, the shaded region indicates unit cell. (b) In-plane bonds, (c) out of plane bonds, (d) two different orientations of carbon atoms. (Source: Dash et al. (2014))

The geometric and atomic structure of graphene is shown in Figure 1.1. In Figure 1.1 (a) the dark and the light circles represent carbon atoms at two different sublattices named respectively as A and B, the shaded region indicates the unit cell. Figure 1.1 (b) shows the sp^2 hybridized orbitals of carbon atoms symmetrically distributed in the molecular plane at angles of forming three σ-bonds with those of the three nearest neighbors. In Figure 1.1 (c) the orbitals of the remaining electrons distributed perpendicular to the molecular plane form π-bonds with those of one of the nearest neighbor, assigning four bonds to each carbon atoms. In Figure 1.1 (d) two different orientations of the arrangement of carbon atoms at lattice sites A and B, the honeycomb lattice can be viewed as two interpenetrating triangular lattices of A and B carbon atoms (Dash et al. (2014)).

The real and momentum space of the graphene lattice can be seen in Figure 1.2(a). The hexagonal lattice of graphene, with the nearest neighbor δ_i and the primitive $\vec{a}_i$ vec-

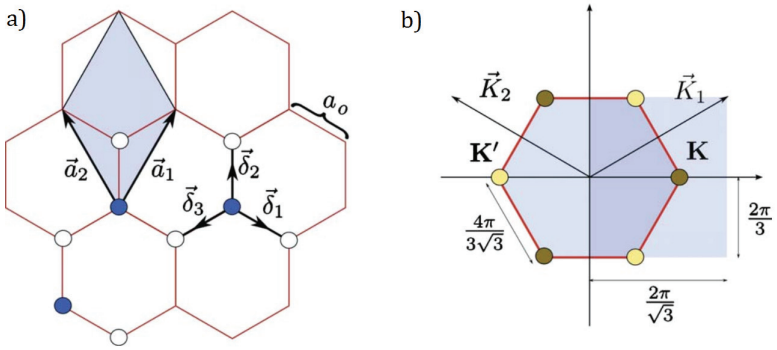

Figure 1.2. (a) Real-space lattice with primitive and the nearest neighbor vectors, and (b) Brillouin zone of graphene. (Source: Peres (2010))

tors depicted. The area of the primitive cell is $A_c = 3\sqrt{3}\, a_0^2/2 \cong 5.1$ Å^2 and $a_0 = 1.42$ Å. In Figure 1.2(b), the Brillouin zone of graphene with the Dirac points $\mathbf{K}$ and $\mathbf{K}'$ were shown. Close to these points, the dispersion of graphene is conical and the density of states is proportional to the absolute value of the energy (1.3). Real space primitive vectors can be given as $\vec{a}_1$ and $\vec{a}_2$;

$$\vec{a}_1 = a\big(1/2, \sqrt{3}/2\big), \quad \vec{a}_2 = a\big(-1/2, \sqrt{3}/2\big) \tag{1.1}$$

where a can be expressed as $a = |\vec{a}_1| = |\vec{a}_2| = \sqrt{3}a_0$. The nearest neighbor vectors as δ_1, δ_2 and δ_3;

$$\vec{\delta}_1 = a_0\Big(\frac{\sqrt{3}}{2}\hat{x} - \frac{1}{2}\hat{y}\Big), \quad \vec{\delta}_2 = a_0\Big(-\frac{\sqrt{3}}{2}\hat{x} - \frac{1}{2}\hat{y}\Big), \quad \vec{\delta}_3 = a_0\hat{y} \tag{1.2}$$

For the reciprocal lattice vectors;

$$\vec{b}_1 = \frac{2\pi}{a}\big(1, \sqrt{3}/3\big), \quad \vec{b}_2 = \frac{2\pi}{a}\big(-1, \sqrt{3}/3\big) \tag{1.3}$$

1.3. Electronic Structure of Graphene

Graphene possesses a striking band structure due to its crystal lattice, where the carbon atoms form a hexagonal honeycomb pattern on a two dimensional plane. Each

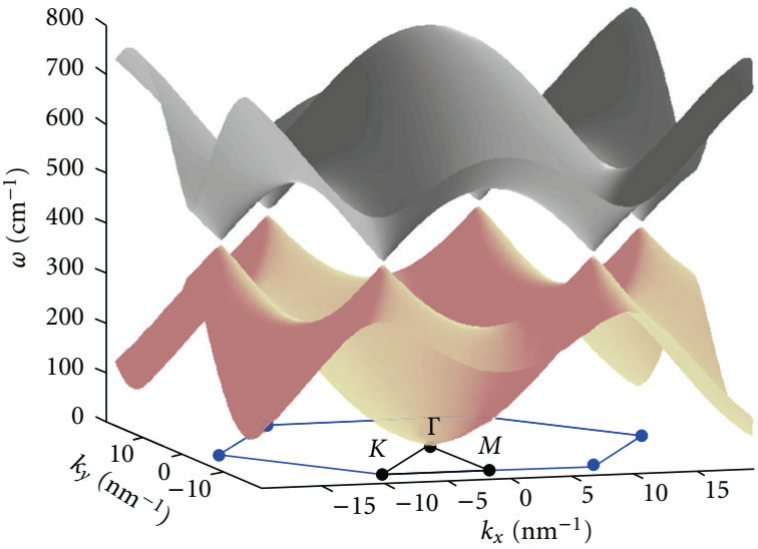

Figure 1.3. First Brillouin zone and band structure of graphene. $\mathbf{K}$ is the corner of the zone, and $\mathbf{M}$ is the midpoint between adjacent nonequivalent corners. $\mathbf{\Gamma}$ is the zone center. Corners are also known as the Dirac points. The Dirac points are the transition between the valence band and the conduction band. (Source: Cooper et al. (2012))

carbon atom is about 1.42 Å far from its nearest neighbours, which it shares a σ bond with each. The fourth bond, π-bond, is oriented at the z-axis and centered on the nucleus, as a pair of symmetric lobes. Each atom in the lattice has one π-bond, which hybridize and form π and π^*-bands. These bands fundamentally form the electronic properties of graphene. Because of its 2D structure, carriers are forced to move in plane and this results with a constrained momentum in two dimensions as shown in Figure 1.3. From the energy versus momentum dispersion relation it can be deductible that the conduction and valance bands of graphene touch each other at the Dirac points. The position of the Dirac points are located at the edges of the Brillouin zone. There are two sets of three Dirac points. These sets are not equal to each other and labelled by $\mathbf{K}$ and $\mathbf{K}'$. We can deduce that the valley degeneracy of the graphene $g_v = 2$. Instead of $\mathbf{\Gamma}$, in graphene both $\mathbf{K}$ and $\mathbf{K}'$ play an important role. Electrons, whose energies are within several meV above or below the Dirac cone can be successfully described with a linear dispersion relation. So, the system can be expressed by the Dirac equation. Because of the effective mass related with the second derivative of the energy to wavenumber, in the linear dispersion regime effective mass of the electrons must be zero. For the expression of the dispersion relation near $\mathbf{K}$

point is:

$$E_{\pm}(k) \approx \pm\hbar\nu_F|k - K| \tag{1.4}$$

which corresponds to the spectrum of the Dirac-like Hamiltonian for low-energy massless Dirac fermions (again in the sublattice basis)

$$H_K = \hbar\nu_F \begin{pmatrix} 0 & k_x - ik_y \\ k_x + ik_y & 0 \end{pmatrix} = \hbar\nu_F \vec{\sigma}.\vec{k} \tag{1.5}$$

The Hamiltonian that is written for the massless Dirac fermions around K is likely to be the tight binding Hamiltonian. $\hbar\nu_F$ can be expressed as $3ta/2$ around K. Around K' Hamiltonian is written as,

$$H_{K'} = \hbar\nu_F = \hbar\nu_F \vec{\sigma^*}.\vec{k} \tag{1.6}$$

where $\vec{\sigma} = (\sigma_x, \sigma_y)$ is the 2D vector of the Pauli matrices (and $*$ denotes the complex conjugate), $\vec{k}$ is the wavevector, and ν_F is the Fermi velocity which is about the $1/300$ of the speed of light in vacuum. Charge carriers in graphene posseses an effective speed of light given by the Fermi velocity and act like massless particles. This enciting phenomenon has so far placed graphene to the hotspot of many research groups. Under electric fields, charged particles accelerate. The limit of the carrier speeds is the mobility. In other words, mobility can be thought as a kind of resistance against the electric field. Despite the very high carrier speeds in graphene, mobility is the restrictor of the carriers. So for the graphene based electronic devices, it is crucial to understand the scattering mechanisms in the structure. Along its massless electrons with very high speeds, it is important to achieve higher mobilities for high-speed electronic devices. There are two possible ways to improve the carrier mobility in graphene: removing the substrate or using a substrate without a trapped charge. The production methods of graphene has advantages and disadvantages about the mobility: Exfoliated graphene has higher mobilities but lower sizes, chemical vapor deposited graphene has lower mobilities but higher sizes, epitaxially grown graphene has higher mobilites and higher sizes, but it is substrate dependent. Researchers still try to find different methods for chemical vapor deposition (CVD) grown graphene to increase the mobility.

1.4. Graphene as a Transparent Conductive Electrode

The simplicity of the electronic band structure of graphene allows us to measure its absorption spectrum. Monolayer graphene is zero band gap semiconductor, so this unique circumstance can be used to study dimensionality effects. Absorption coefficient in the infrared regime is exactly $\pi\alpha \simeq 2.3 \pm 0.10\ \%$, where $\alpha = e^2/\hbar c$ is the fine structure constant. For the visible range, the factor for correction is around $3\ \%$.

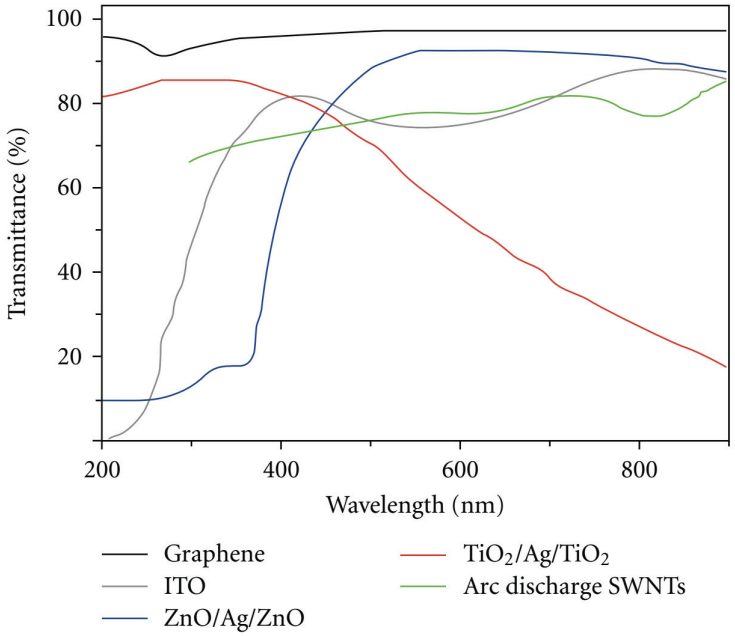

Figure 1.4. The transmittance of transparent conductive electrodes that are used commercially for UV, visible and NIR regimes. (Source: Bonaccorso et al. (2010))

The UV-Visible-NIR spectrum of the graphene shows an excellent optical transparency in the ultra-violet and the visible regions. Thus, this property makes graphene a perfect candidate to be used as transparent conductive electrode (TCE) for optoelectronical applications. Conventionally, contemporary research uses Ni/Au, Ti, TiW and indium tin oxide (ITO) based transparent conductive electrodes for solar cell and photodetector applications. However, these structures transparency fail in the wavelengths below $400\ nm$ as seen in Figure 1.4. In this manner, graphene stands unrivaled candidate to be implemented as transparent conductive electrodes both in photovoltaic devices, and

in photodetectors that are meant to work in the UV region, as this 2D material has a transparency of over 90 percent in the region between $200 - 400\ nm$. Although there are many application for the graphene as a metal electrode for metal-semiconductor-metal (MSM) and metal-semiconductor (MS) photodetectors, it still needs to be improved.

1.5. Photocurrent Spectroscopy

The Photocurrent Spectroscopy (PS) is a powerful technique to investigate the electrical response of materials to incident light. Excitation occurs from valance band to conduction band as well as the defect and trap states under sufficient irradiation energy. Therefore, an increment is measured in the current with the contribution of the photogenerated carriers. By using PS, it is possible to conduct two different transition properties of the materials: In the first case wavelength-resolved PS ensures to examine the interband and band-to-band transitions (Figure 1.5 (a)), while in the second case the time-resolved (transient) PS provides the grow and decay time of the photoexcited carriers (Figure 1.5 (b)). The transient photocurrent spectroscopy (TPS) is commonly used to study surface trap states induced by adsorbates.

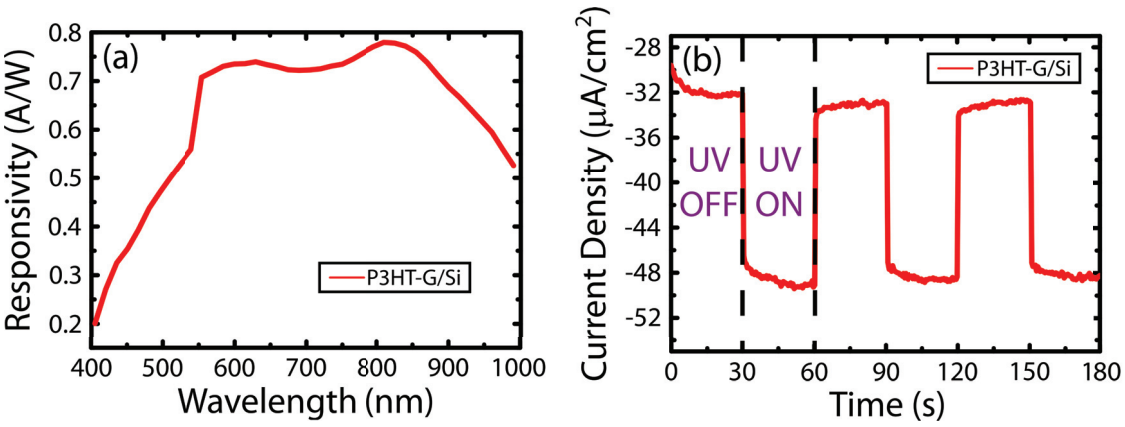

Figure 1.5. The (a) wavelength-resolved, (b) time-resolved photocurrent spectroscopy measurements of P3HT-Graphene heterostructure.

1.6. Interaction of 2D Materials with Atmospheric Adsorbates

Owing to their superior surface-to-volume ratios and hence their sensitivities to extrinsic adsorbates, 2D materials are considered to be adapted for gas and humidity sensing technology. However, this unique property of 2D materials present serious problems when they are desired to be used as an electrically stable component in electronic and optoelectronic device applications. The adsorbates like O_2 and H_2O in the atmosphere serve as surface trap states and thus strongly alter the charge carrier transport characteristics of these 2D materials. This interactions are probed overly for ZnO, which has a wide band gap of $3.37\ eV$. Thus, this makes ZnO one of the fundamental candidate for UV based thin film and nanowire photodetectors. In order to understand the device performance of ZnO based UV photodetectors, TPS characteristics must be investigated.

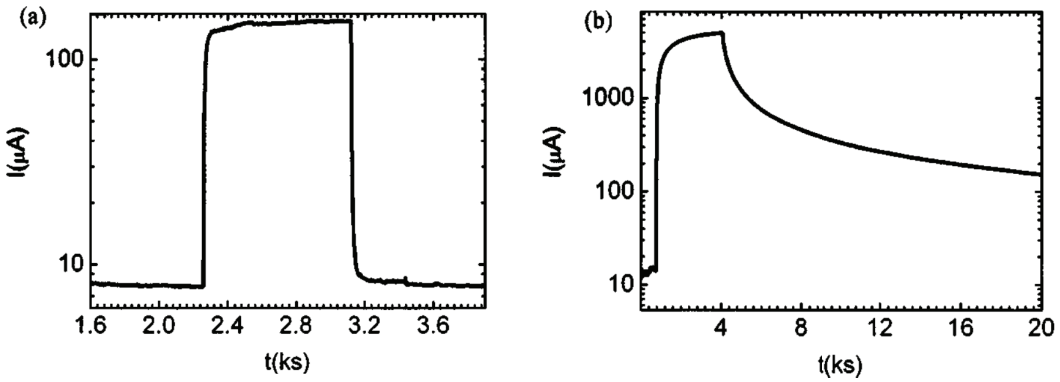

Figure 1.6. The TPS measurements of ZnO thin films (a) in atmospheric conditions and (b) in vacuum conditions under UV illumination. (Source: Li et al. (2005))

Li et al. (2005) investigated the TPS characteristics of ZnO based nanowire films which are shown in Figure 1.6. The on/off periods of the samples are taken a very long time (around $400\ s$) in atmospheric conditions (Figure 1.6 (a)) to reach the saturation or its base current conditions, even though it could not reach the base currents (after $20\ ks$) in vacuum (Figure 1.6 (b)). This is because of the vapor pressure of the oxygen gas and water vapor are diminished in vacuum. Thus, the adsorbate amount is greatly reduced. This clarifies the unachieveable base equilibrium in vacuum. On the other hand, the exceedingly time dependent response of samples interpret the conductivity alteration strongly

depends on the adsorption/desorption processes, whereas it is supposed to depend on photogenerated charge carriers.

As we know from literature, the oxygen vacancies in ZnO thin films which eventuates in growth process cause uncontrollable electron doping. This results with unintentional n-type doped ZnO thin films. With TPS measurements, it can be seen obviously from Figure 1.6 (a) that the desorption under UV illumination leads to an increment in the measured current. With the results, it has been implied that the atmospheric gases act as electron trapper in the surface of thin films. Thus, researchers are focused on the moisture and gas sensing properties of ZnO thin films and nanowires due to its electrical instability. The characteristics of typical moisture sensor based on ZnO nanowire is investigated by Li et al. (2009) and the results are shown in Figure 1.7.

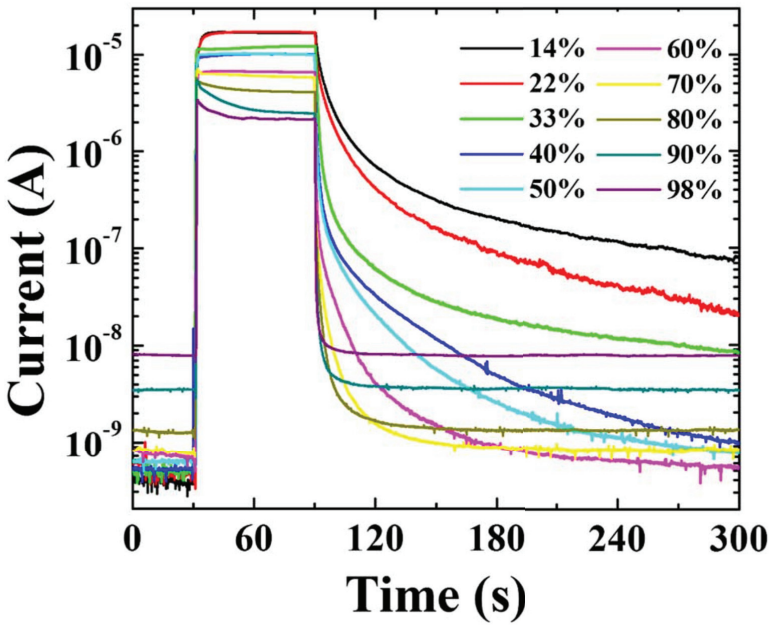

Figure 1.7. The conductivity variation of ZnO based humidity sensor under different moisture concentrations. (Source: Li et al. (2009))

Moisture ratio of the atmosphere effects the conductivity of the ZnO based sensor as desired, but the reset time, which is the required time to turn to initial conditions of device strongly depends on the moisture ratio: Lower the moisture, longer the reset time. Also it is deductible that the sticking rate depends on time exponentially. So the efficiency of the device must be improved to adapt it to sensor technology.

One of the recently popular metal dichalcogenides MoS_2, which also has an enor-

mous surface-to-volume ratio, can be given as an example for the interactions with atmospheric gases. Jariwala et al. (2013) has showed that the MoS_2 field effect transistor changes its characteristics depending on the ambient conditions. The doping concentration of MoS_2 layer dramatically alters with the adsorbates. To achieve same source/drain current, -70 V in vacuum should be applied, whereas -20 V is needed in ambient conditions. This difference in the gate voltage emphasises that the adsorbate strongly alters the electrical characteristics.

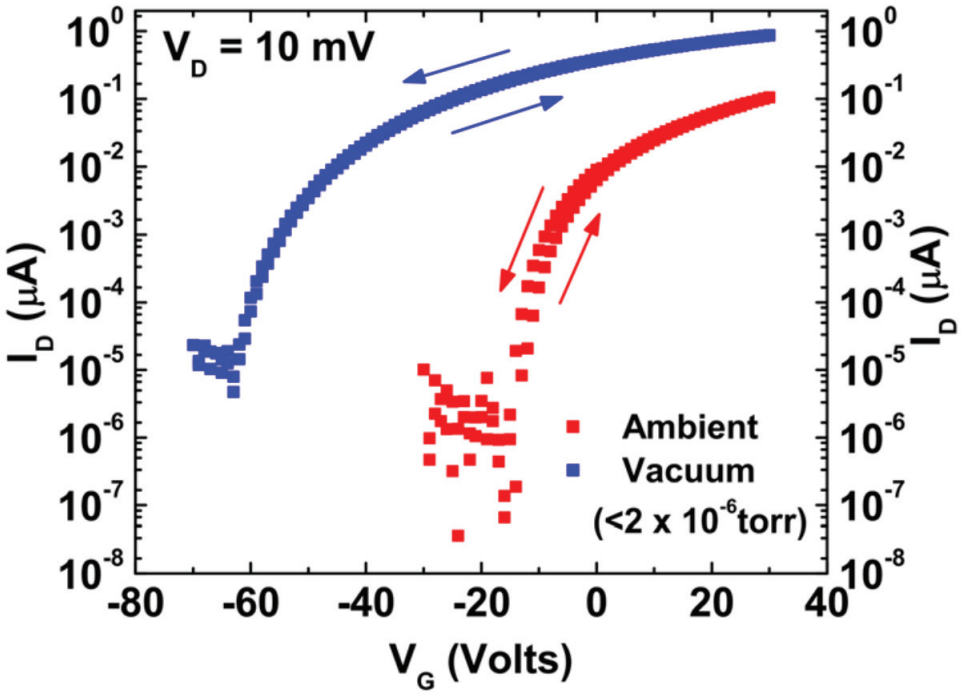

Figure 1.8. The adsorbate dependent variation of source/drain current. $V_{g,min}$ is shifted due to the ambient doping. (Source: Jariwala et al. (2013))

1.7. Motivation

In this thesis, we developed an experimental model to reveal the effect of adsorption/desorption of atmospheric adsorbates on the electronic and optoelectronic characteristics of graphene layers with two different conductivity types on SiC substrates. In-vacuum TPS measurements, taken under $254\ nm$ UV light illumination, showed that the adsorbates greatly modify the photocarrier generation/recombination processes in the samples depending only on the carrier type of graphene layer. For comparison, a set of graphene/SiC samples with two different carrier types were encapsulated by $100\ nm$ thick SiO_2 film using Pulsed Electron Deposition (PED) and Thermal Evaporation (TE) techniques. We observed an improvement of supressing the adsorbate interactions after the thermal encapsulation, however rectified and sharp transitions could not be achieved. We found that the photoresponse time of bare graphene/SiC samples was drastically reduced (independent of graphene carrier type) from hours to a second when their surfaces are passivated by PED. The experimentally obtained results are used to clarify the material-independent mechanism behind the interactions adsorbents and surface, that becomes more of an issue when using 2D materials as electrically stable component in electronic devices.

CHAPTER 2

SURFACE ADSORPTION IN 2D MATERIALS

Material surfaces are one of the most important parts of the material science. Each hypothetical reciprocal action to provide the lowest energy state for them is unattainable, therefore the energy of the molecules and/or the atoms at the surface is greater than the energy associated with the bulk. In addition to this added convenience, another benefit would be the fact that due to the greater energy, reactions and interactions occur on the surface. The interaction between the surface and an approaching molecule causes the energy of the system to diminish at once. The adherence process of the atom or the molecule at the interface between two bulk phases is called adsorption. Described as adsorpt or adsorptive (Figure 2.1) before the adherence process, the attached chemical is referred to as the adsorbate while the most strongly adhered bulk phase is called the adsorbent. The quantity of the adsorpt to eventually attach the adsorbent depends on the concentration or the vapor pressure of the adsorpt and the system temperature.

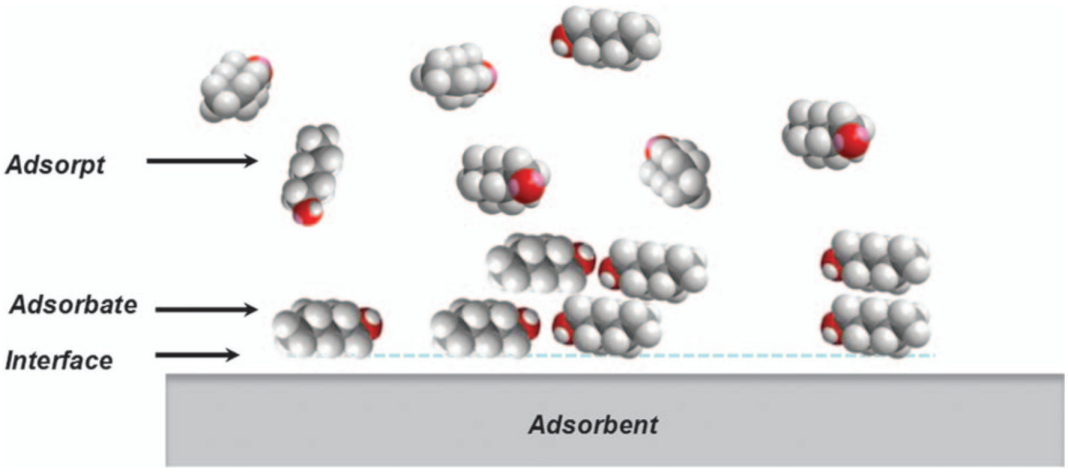

Figure 2.1. The schematic point of view of adsorption process with its terminological components. (Source: Gross (2014))

The adsorption studies play an exclusive role in the surface science field. The adsorption processes are relevant in nearly every technological system where material surfaces are of pivotal importance such as the preparation of a device (i.e. a semiconductor device) or the industrial processes like heterogeneous catalysis in which the reactants need to adsorb on the catalyst to be able to create a reaction. Furthermore, the physical and chemical factors that affect the adsorption process are the most intriguing when observed from a fundamental point of view.

2.1. Potential Energy Surfaces

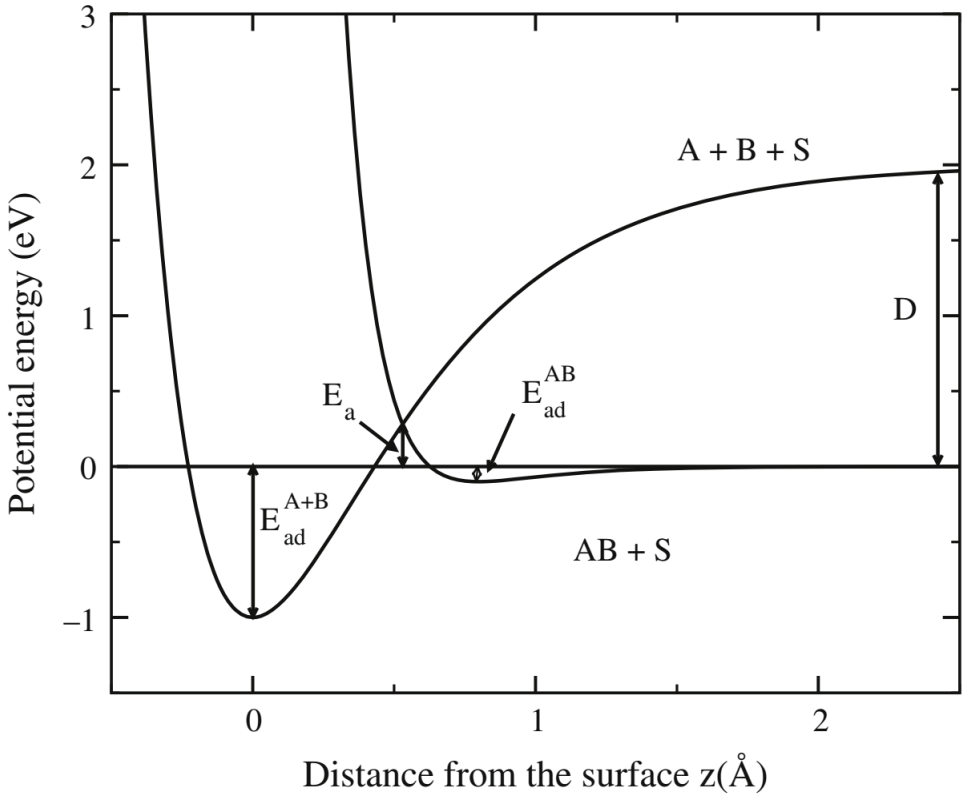

Figure 2.2. The molecular and dissociative adsorption potential curves in conformity with Lennard-Jones potential. (Source: Gross (2014))

The potential energy surface (PES) of the system is the main quantity to be considered when a theoretical description of adsorption is needed. The PES is correlated with the energy hyperplane concerning the configuration space of the atomic coordinates

of the related atoms. The data on sites and energies of adsorption, vibrational adsorbate frequencies, reaction paths, and the presence of any barriers for adsorption, desorption, diffusion and reactions is provided by the PES. In the surface science field, adsorption has long been described by one-dimensional potential curves, the most pre-eminent of which can be traced back to Lennard-Jones and is shown in Figure 2.2. Two curves are shown in this figure: the curve $AB + S$ reflects the potential energy of the molecule AB approaching the surface S. The shallow minimum E_{ad}^{AB} can be observed before a sharp rise occurs in the curve. Meanwhile the second curve, $A + B + S$, correlates with the interaction between the two distant atoms A and B and the surface. While far removed from the surface, the energetic difference D between these two potential curves is the equivalent of the dissociation energy of the free molecule shown as AB. Having two separate atoms instead of the intact molecule to interact with the surface is far more convenient in energy terms while close to the surface. This situation is a good example of a dissociative adsorption scenario in which the energy gain regarding the molecule AB is shown as E_{ad}^{AB} while the energy gain after the adsorption of the separate atoms A and B is displayed by $E_{ad}^{AB} + D$ (Gross (2014)).

Where the crossing point is between the curves $AB + S$ and $A + B + S$ reveals if there is a barrier for the dissociative adsorption. Figure 2.2 depicts the activated dissociative adsorption and the diabatic dissociation barrier E_a. Because of the avoided crossing between the adiabatic potential curves, the adiabatic barrier will be slightly lower. If the crossing of the two curves occurs closer to the surface and thus at a potential energy $< 0\ eV$, the molecule can dissociate spontaneously at the surface and leave us with a non-activated dissociative adsorption.

Potentially achievable curves similar to those in Figure 2.2 depict the energetics regarding the adsorption process. Nonetheless, assuming that we do not have any additional information, this does not present us with the facts related to the physical and chemical state of given interaction between the adsorbates and the surface. The shallow molecular adsorption well shown in Figure 2.2 usually corresponds to a physisorption well caused by van der Waals attraction while the steep rise of the potential energy is due to the repulsion between electrons. For the said chemisorption, corresponding to the true chemical bonds being created between the adsorbate and substrate, the gained energy as a result of the dissociative adsorption process is commonly seen. Mentioned interaction can also be split into categories as ionic, metallic or covalent bonding.

As commonly known, the dry air consists of mostly nitrogen as $N_{2_{(g)}}$ $(78\ \%)$ and oxygen as $O_{2_{(g)}}$ $(20\ \%)$. Wet air has the additional H_2O in vapor phase. Therefore it is

crucial to study the adsorption properties of the nitrogen gas, the oxygen gas and the water vapor to achieve the ambient conditions for our surface properties. Now, the situation arises: what is the type of adsorption? The problem encountered while differentiating between chemisorption and physisorption is quite similar to the one between chemical and physical interaction in general.

2.2. Physical Adsorption (Physisorption)

The adsorbate is referred to as a physisorbed in the case that the molecules create a reversible bond with an adsorbent and can freely diffuse over the adsorbent without forming any strong bonds. The sublimation energy of a molecule which is adsorbed onto the said surface is of the order of that are needed to ensure that the typical non-covalent interactions will break. Van der Waals interactions are especially significant in verifying if the molecules will be physically adsorbed to a surface. Utilizing non-covalent interactions between adsorbate molecules can specify this reversible attachment process of the molecules onto a surface.

When a chemical bond between the adsorbate and the surface is not established, the adsorption form will be at its weakest state. The bonding occurs as a result of the interaction between an induced dipole moment of a non-polar adsorbate and its image charges in the polarizable solid. This conveys the fact that Van der Waals forces brings about the said attraction. The sublimation energy, which is roughly calculated as $0.02 - 0.04\ eV$, belonging to a molecule which is absorbed onto the said surface is similar to the needed amount to break the typical non-covalent interactions. Even for an interaction relatively as long as 3 Å to 10 Å, it indeed plays a vital part in the bonding process. We are mostly interested in the Van der Waals interaction of rare gases and molecules with filled electron shells with surfaces considering that it is the key attraction between these species and surfaces. The Van der Waals term is considered to be "one and the same" with physical adsorption, however, its use is highly discouraged. Distinctively, physisorption does not include an important change in the electronic orbital patterns for the species in question.

There are some characteristics that help us understand whether the absorption is physical. First of all, the physisorption is general and can take place in any solid or fluid system. Yet some specific molecular interactions, due to the geometrical and/or electronic characteristics regarding the adsorbent and/or the adsorptive, may arise. Additionally, the evidence as to the perturbation of the electronic states the adsorbent and

the adsorbate is at the lowest point as their bonding energy is in the order of meV. The adsorbed species and the ones in the gas phase are completely identical in the chemical nature. Therefore, the adsorption and the following desorption does not affect the chemical properties. The interaction energy that occurs between the adsorbate molecules and the adsorbent is at the same order of magnitude as or higher than the condensation energy belonging to the adsorptive. Another characteristic is that the first step does not necessitate an activation energy when a gas phase undergoes a physical adsorption. Nevertheless, the rate-determining processes of transportation may cause slow, temperature dependent equilibration. Equilibrium is established between the adsorbate and the gas phase during the physical adsorption process. The extent of this physical adsorption rises as the gas pressure rises and drops as the temperature drops in solid or gas systems if the pressure is not too high. Metastability can be seen in the equilibrium if the systems display hysteresis. If the necessary pressure and temperature conditions are met, molecules from the gas phase may be adsorbed more than the ones which are directly in contact with the surface (multilayer adsorption or filling of micropores) (Gross (2014)).

2.3. Chemical Adsorption (Chemisorption)

Possible chemisorbed structures are created as a result of particular strong bonds forming between a surface and an adsorbed molecule. These structures usually differ greatly from the physisorbed systems in structure and chemistry. Chemisorption is likely to form mostly imperfect structures due to the fact that the results of the adsorption process are mainly determined kinetically. When surface atoms and an adsorpt create a bond, it is difficult to encounter a movement between them. However, the monolayers in question are significantly more potent than the physisorbed layers in that the bonds between the adsorbent and the adsorbate are relatively stronger. The local bond linking the two layers together and the geometric restrictions leads to the molecule′s orientation to be in any direction as long as the other bonds in the same adsorbate molecule allows it. The interaction between the high majority of adsorbates and the surface would be weak, non-covalent and at a distance from the strong bond when the coverage is low. To put it in a different way, “physisorbed” is the part of the adsorbate which is far away from the location of the covalent bond. It may have mobility; however, it can not escape from its environment. It can pile up next to the connection point of the molecule when the temperature is low. However, when the coverage is high, the molecules would tend to align perpendicular to the plane of the surface of the adsorbent in a way that the maximum

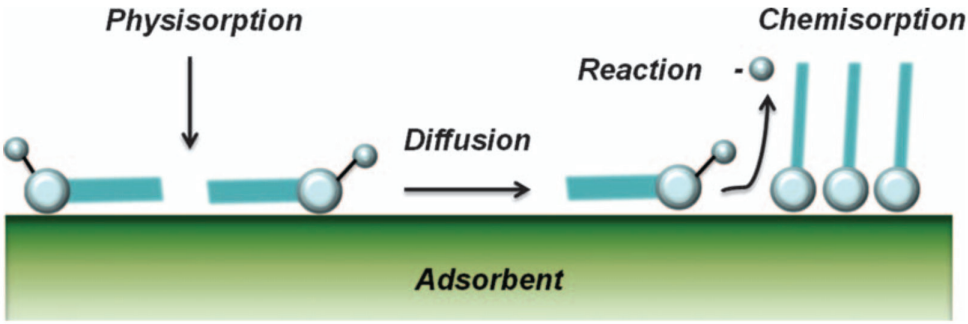

Figure 2.3. The transition from physisorption to chemisorption: Adsorbate sticks to the surface and diffuse with its thermal energy. After reaction with the charges of the surface it becomes chemisorbed. (Source: Grill (2016))

number of strong bonds can be made by the surface atoms of the adsorbent. The type of adsorption where the forces are valent and similar to the ones that work in the formation of chemical compounds is called chemisorption. The bonds in chemisorption are specific, such as covalent, ionic, metallic. Chemisorption is only for the surface symmetry, which is different from the physisorption. The bonding energy in chemical adsorption is in the order of several eV and has relatively short interaction length as 1 Å to 3 Å.

Physisorption typically constitutes the first step in the chemisorption process. The molecule sticks to the surface, yet it still can diffuse in the plane as allowed by the substrate temperature, which was illustrated in Figure 2.3. This can be overtly seen when molecules are adsorbed onto surfaces from the vapor state under vacuum conditions. Additionally, the layer growth should be affected kinetically due to the relatively slow diffusion of the molecules. There are some characteristics that reveal whether the absorption is chemical or not, as in the case of physisorption.

The chemical specificity characterizes the chemisorption phenomenon. By using the appropriate physical tools such as UV, infrared or microwave spectroscopy, electrical conductivity or magnetic susceptibility, we can detect the changes that occur in the electronic state of samples. The surface dissociation or reaction may cause some chemical changes in the adsorptive and attaining the original species on desorption may be impossible. In these instances chemisorption may be irreversible. The chemisorption energy belongs to the same order of magnitude similar to any other chemical reactions that occur between a fluid and a solid. Therefore chemisorption, as other chemical reactions, can be exothermic or endothermic. The magnitudes regarding the changes in the energy also can

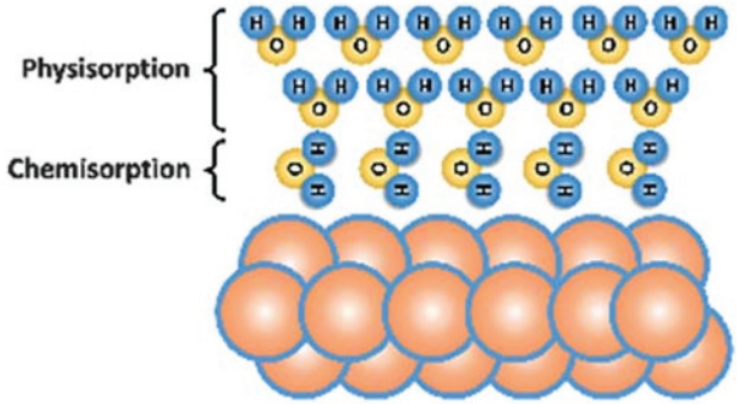

Figure 2.4. A schematic view of both adsorption mechanisms: stuck multilayer physisorbed water molecule upon monolayer chemisorbed water molecule. (Source: Xia et al. (2014))

vary from very small to very large. The first step in chemisorption usually requires an activation energy. In the event that the activation energy is large (activated adsorption), true equilibrium is either attained over a long course of time or never attained in practice. For instance; while examining the adsorption of gases by solids, the observed adsorption may increase as temperature goes up, if a constant gas pressure is provided for a certain period of time. Moreover, if a large amount of activation energy is needed for desorption, subtracting the chemisorbed species placed on the surface might only be possible if certain extreme conditions for temperature or high vacuum are met or if the surface undergoes an appropriate chemical treatment. As the bonds between the adsorbed molecules and the surface are valence bonds, the molecules will gather on certain areas of adsorption and a single layer of chemisorbed molecules (monolayer adsorption) will be constituted.

2.4. Adsorption on Graphene

Since it has a superior surface-to-volume ratio, graphene is one of the strongest candidate for gas sensing applications. Schedin et al. (2007) are investigated the gas sensing capability of graphene layer under different gas conditions (Figure 2.5). Although the measured resistivity is influenced under NH_3, CO, H_2O and NO_2 gases, reaching the saturation is completely dependent to the type of the gas. It can be seen that the saturation

of the resistivity can only be achieved after $500\ s$ under NO_2 gas. This means reaching the saturation is completely dependent to the type of the gas. Resetting the device is also a time dependent process. Higher saturation level causes longer resetting time.

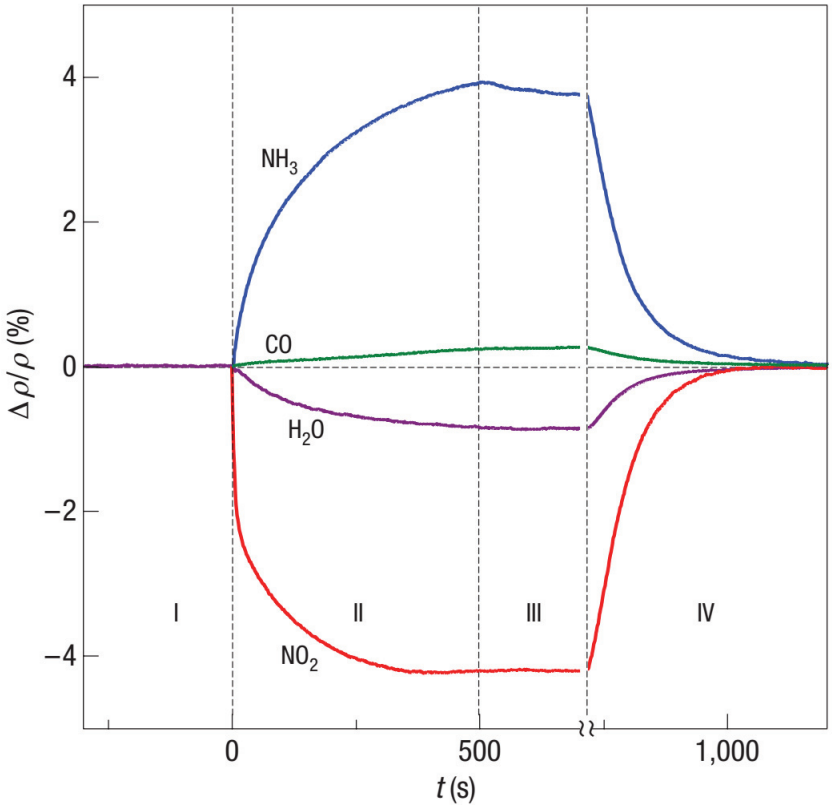

Figure 2.5. The resistivity variations of graphene under different gas concentrations. First part is the initial conditions under vacuum. Second part is the gas exposure region. Third part is relaxation part under vacuum. Forth part is annealing part to recover initial conditions. (Source: Schedin et al. (2007))

One important study related to the adsorption/desorption processes on graphene layer is done by Ryu et al. (2010) by using micro-Raman spectroscopy method. The compressive strain and electrical doping generally contribute together to G band shift ($1580\ cm^{-1}$), although environment-controlled in situ Raman spectroscopy measurements showed that the observed increment in both pristine and annealed graphene is principally due to O_2 induced hole-doping rather than in-plane compressive strain.

First of all, sample is annealed for two hours at $290\ ^{\circ}C$ under flowing Ar to determine the contribution of the compressive strain on G band shifting. $\Delta\omega_G$ measured under

Ar atmosphere (Figure 2.6 (ii)) The shift was $1.5\ cm^{-1}$ higher than in the initial state at $23\ ^{\circ}C$ (Figure 2.6 (i)). The change in measured $\Delta\omega_G$ corresponds to $0.12\ \%$, which can be admitted upper limit for the compressive strain upon annealing. Afterwards, G band increment is investigated under dry O_2 gas to examine the O_2 contribution. Measurements are done consecutively at one spot (Figure 2.6 (iii)) as a function of O_2 exposure. Then, Ar is replaced with O_2 to recover the initial conditions, the recovery time is around a couple of minutes. The total shift in measured $\Delta\omega_G$ was around $4\ cm^{-1}$. They concluded that O_2 binds on or near the annealed graphene causing a hole doping of $2 \times 10^{12}/cm^2$. After additional two-hour annealing at $320\ ^{\circ}C$ in Ar, sample is exposed to dry O_2 again and induced an even larger blueshift in $\Delta\omega_G$ ($7\ cm^{-1}$). Unfortunately, the gases in ambient conditions are wetted. Thus, the impact of the wetting should also be examined. In Figure 2.6 (vii and viii) sample is exposed to wet N_2 and wet O_2, respectively. While there is no change observed G band shift under wet N_2, a drastic change is observed under wet O_2. Moreover, it became impossible to recover initial conditions even under dry Ar.

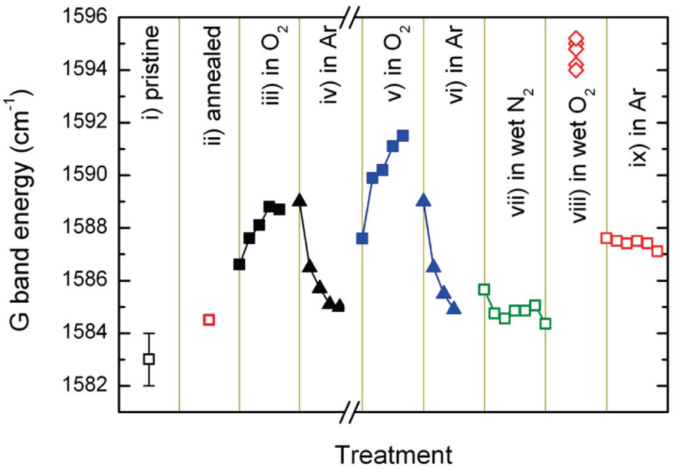

Figure 2.6. The G band shifting of graphene layer under different conditions: under O_2, Ar, wet O_2 and N_2. (Source: Ryu et al. (2010))

Graphene forms a Schottky junction when it is transferred onto most of the conventional semiconductors like Si, GaAs and SiC (Tongay et al. (2009), Tongay et al. (2011), Chen et al. (2011)). Because of the fact that graphene/semiconductor heterojunction is expected to reveal a strong rectification which can be utilized for Schottky barrier devices like tunneling field effect transistors, photovoltaics and photodetectors with relatively low leakage currents at the level of nA (An et al. (2013)), even at pA (Li et al.

(2016)). However, Ryu et al. (2010) showed that the adsorbate induced alteration in graphene′s carrier concentration yields undesirable variations, also in the effective Schottky barrier height (which is investigated by Nomani et al. (2011)) and thus gives rise to instabilities in the device performance. Yang and Murali (2011) are revealed the conductivity alteration of graphene under atmospheric gas exposure. The density of charge carriers (electrons and holes) in the transistor can be tuned by applying an electric field to the gate of the device. Along with the sticking of adsorbate, the conductivity of the GFET (Graphene Field Effect Transistor) varies under the same gate potential due to the additional doping. For similarity, only the single layer graphene will be discussed.

Back-gated IV characteristics are extracted every $30\ s$ for each sample. The chamber is vacuumed to its base pressure, then exposed O_2 by a flow meter and brought to atmospheric pressure (a kind of an ventilation of chamber by O_2). In equilibrum chamber is opened to the ambient and the ambient exposure begins. In the SLG case, $V_{g,min}$ increases rapidly during dry oxygen exposure. This positive increment of $V_{g,min}$ gives rise to hole doping. The accretion of $V_{g,min}$ greatly increases after ambient exposure, which is shown in Figure 2.7 (a). It is clear that the hole doping continues under atmospheric gases. The shift in $V_{g,min}$ indicates a net hole transfer of $5 \times 10^{11}\ cm^{-1}$ after dry oxygen exposure for nearly $1\ h$. The minimum conductivity σ_{min} exhibits a complex behavior with doping and the number of graphene layers. Figure 2.7 (b) shows the change in σ_{min} over the course of oxygen and ambient exposure, defined as $(\sigma_{min} - \sigma_0)/\sigma_0$, where σ_0 is the minimum conductivity of the sample in vacuum.

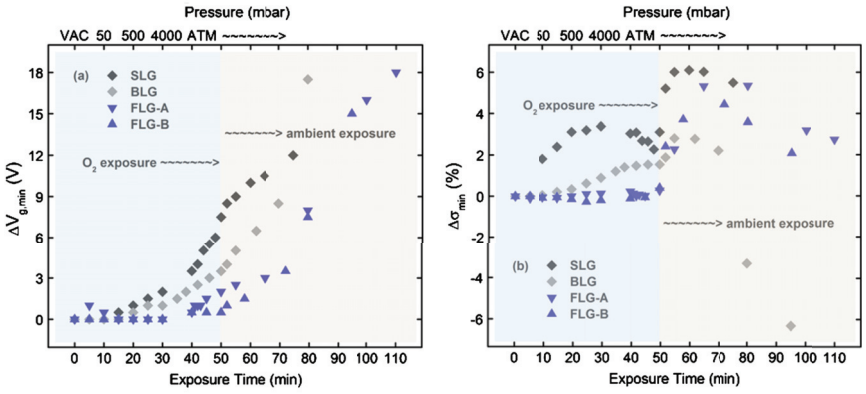

Figure 2.7. (a) $V_{g,min}$ increment of the oxygen and ambient exposed single layer graphene layer. (b) The conductivity of the single layer graphene increse under O_2 exposure after vacuum. (Source: Yang and Murali (2011))

In the case of SLG, σ_{min} increases gently until $500\ mbar$ pressure of O_2 exposure, but then saturates and is continuous with a gradually decrement upto ambient exposure. Afterwards, SLG again shows a sharp initial increase under $5\ min$ ambient exposure, then a saturation for $10\ min$ is followed by a slow falling in σ_{min} for the rest. Yang and Murali (2011) are also investigated the N_2 dependence in place of O_2 (as a simulation of atmospheric gas effect) and not a significant change in conductance characteristics is observed after $1\ h$ of exposure. This finding, combined with the results from oxygen and ambient doping, indicates that oxygen and moisture are the primary species in the atmosphere responsible for doping graphene and is consistent with previous observations.

CHAPTER 3

EXPERIMENTAL

3.1. Preparation of CVDG/SiC and EG/SiC Samples

For our measurements, we used $250\ \mu m$ thick semi-insulating (SI) 4H-SiC substrates purchased from NovaSiC, which are diced into $4\ mm \times 10\ mm$ rectangular pieces. The substrates were cleaned chemically in an ultrasonic bath: acetone, isopropanol and deionized water, respectively. The natural oxide layer was also removed by an HF solution which was $6\ \%$ diluted. CVD grown graphene was transferred from Cu foil onto SI-SiC substrate whereas epitaxial graphene was grown directly on SI-SiC substrate by high temperature vacuum annealing process.

3.1.1. Growth of Epitaxial Graphene on SI-SiC Substrate

Ultra High Vacuum (UHV) is the essential property of growing high quality epitaxial graphene. The base pressure of our lab-built UHV chamber (shown in Figure 3.1) is around $10^{-10}\ mbar$. The temperature measurements of the sample were carried out by a pyrometer with a temperature resolution of $\pm 1\ ^{\circ}C$. Chamber was equipped with two pumps: scroll pump and turbo molecular pump (TMP). As the rough pumping, a scroll pump was used to protect TMP from the ambient pressure. Until a pressure range of $10^{-2}\ mbar$, the scroll pump was utilized to evacuate the rough pressure inside the chamber, then TMP was started to ramp up to vacuum deeply. The pressure of the chamber was traced by a cold cathode gauge controller. The growth of epitaxial graphene was based on the evaporation of Si atoms from the surface of the SiC under high temperatures. Si atoms evaporate at a temperature aabout $1400\ ^{\circ}C$, whereas C atoms evaporate at a temperature of about $3000\ ^{\circ}C$. This temperature difference allows us to vaporize the Si atoms at $1400\ ^{\circ}C$, while keeping the C atoms left at the surface. C atoms that remain at the surface of SiC form graphene when the sample is quenched. Thus, a user friendly sample stage was designed, and can be seen in Figure 3.2.

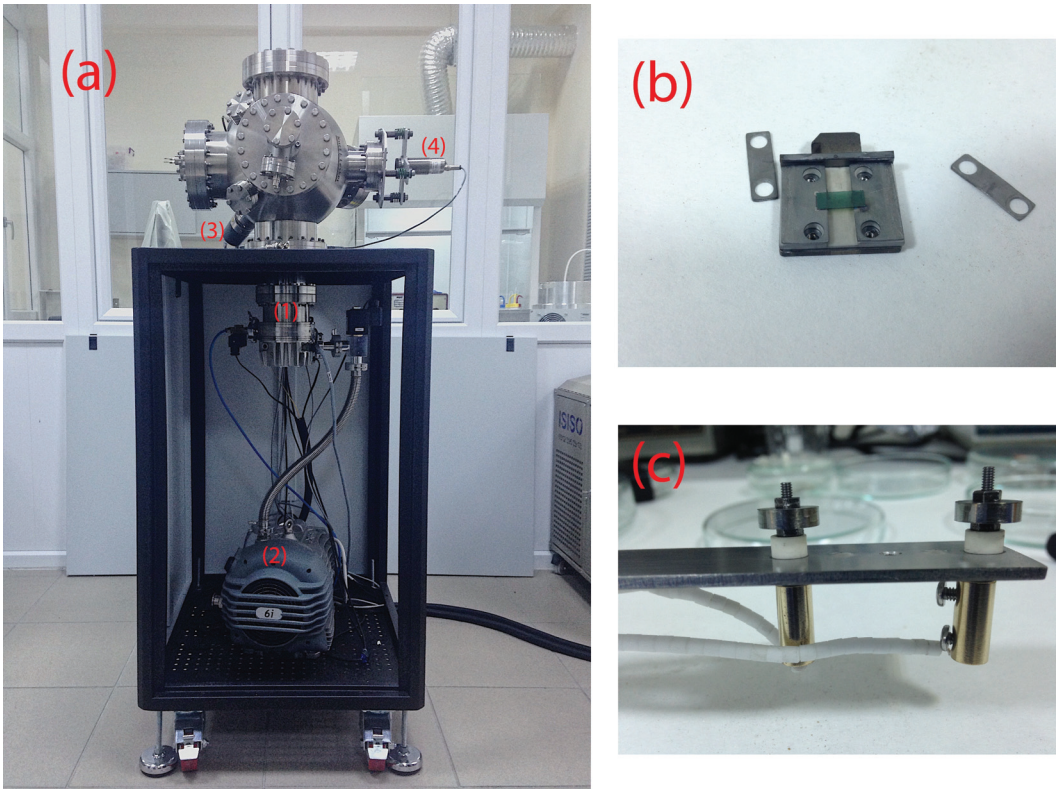

Figure 3.1. The UHV Chamber Setup in Quantum Device Laboratory. It consists of a (1) TMP, (2) a scroll pump, (3) a gauge controller, (4) a pyrometer and electrical connection units. (b) The sample stage of SiC substrates. The tantalum caps for fixing the substrate to its slot with screws. After fixing substrate, sample stage is slided to holder (c) and tightened to electrical ports. Holder head has a CF flange which is competible with UHV Chamber.

For the design, long-wearing and high temperature compatible materials were used: Alumina ceramic as an electrical insulator, tantalum as metallic contacts for source and drain. For the growth, we used Joule heating method, which is a resistive heating method based on driving high currents to produce high power outputs to heat the sample. But for a SI substrate, this method is useless due to the highly resistive structure. To overcome this problem, firstly we grew graphitize n-type SiC substrate with proper growth parameters. Therefore, graphitic n-type SiC substrate could be used as a basic resistor. When we combined the graphitic SiC substrate and the SI-SiC on top of it, it was possible to drive current from graphitic SiC substrate. Thus, graphitized SiC can be heated up with increasing the current. This gave rise to indirectly heating of SI-SiC. The temperature of the SI-SiC substrate can be controlled by the driven current of graphitized SiC. The opti-

mized parameters for growth of graphitized n-type SiC and monolayer epitaxial graphene (MEG) on SI-SiC are given in Table 3.1 and Table 3.2, respectively.

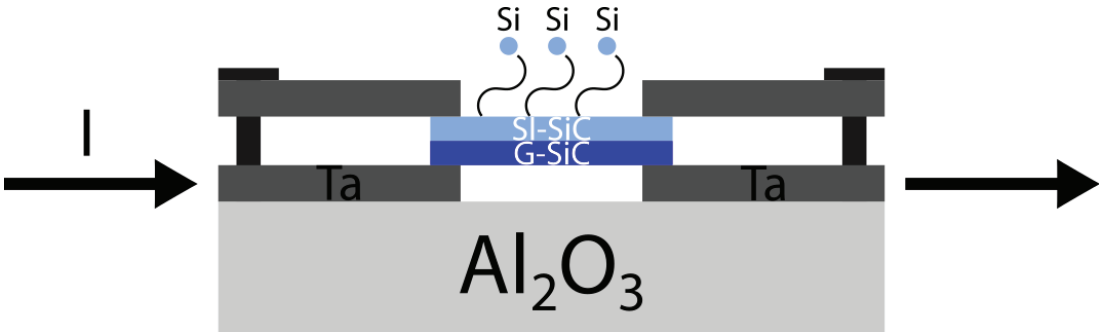

Figure 3.2. The illustration of capping method for the growth of SI-SiC.

Table 3.1. Optimum growth parameters for graphitic SiC heater.

Growth	Thermal Cleaning	Oxide Removal	Surface Preparation	Growth
Degree ($^{\circ}C$)	600	1050	1300	1400
Time (min)	180	10	7	6

Table 3.2. Optimum growth parameters for monolayer epitaxial graphene on SiC

Growth	Thermal Cleaning	Oxide Removal	Surface Preparation	MEG Growth
Degree ($^{\circ}C$)	600	1050	1300	1400
Time (min)	180	10	7	10

3.1.2. CVD Growth and Transfer Process of Graphene

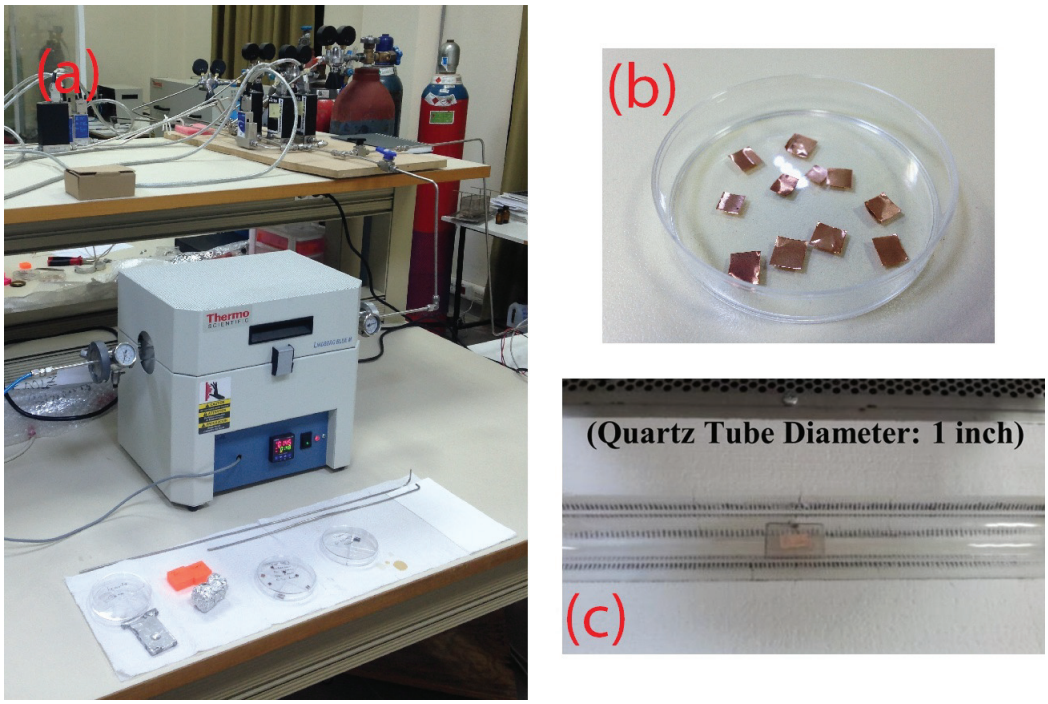

Figure 3.3. (a) The CVD graphene production setup: The furnace has a quartz tube inside to heat up substrates $1100\,^{\circ}C$. Thermocouple to control temperature, flowmeters to control gas flow precisely. (b) pieces of copper foils were diced and prepared for the growth of graphene. (c) Cu substrates has diced into preferred pieces to grow graphene. Quartz wafer helps to hold Cu substrate. Quartz tube can be heated up homogeneously with the help of spiral resistors.

Cu foil ($25\ \mu m$ thick, 99.8 purity, Alfa Aesar) as catalyst-substrate material was placed on a quartz plate and inserted to the tube furnace of atmospheric pressure CVD system (Figure 3.3). As for the first step, the Cu foil was heated up to $1073\,^{\circ}C$ under a H_2 ($20\ sccm$) + Ar ($1000\ sccm$) gas mixture with a temperature ramp rate of $30\,^{\circ}C\ min^{-1}$. Then the foil was annealed under the same temperature and flow rates for one hour. After the annealing process, CH_4 ($10\ sccm$) was introduced into the tube furnace for one minute in order to facilitate the graphene growth. Finally, the sample was left for rapid cooling from growth temperature to room temperature under gas flows of H_2 ($20\ sccm$) and Ar ($1000\ sccm$). Growth chart is given in the Table 3.3.

Microposit S1318 Photoresist (PR) was utilized as the supporting layer during the

Table 3.3. Optimum growth parameters for CVD graphene: Temp; temperature, RT; ramp time, AT; annealing time, GT; growth time.

Temp ($^{\circ}C$)	H_2 (sccm)	Ar (sccm)	CH_4 (sccm)	RT (min)	AT (min)	GT (min)
1000	20	1000	8	30	60	1

graphene transfer process. We drop casted the PR on graphene-Cu template and annealed it at $70\ ^{\circ}C$ overnight. Iron Chloride ($FeCl_3$) solution was used to etch the Cu foil and to suspend graphene-PR. After the Cu foil fully etched away, graphene-PR was rinsed by deionized water to remove $FeCl_3$ residues. After N_2 drying process, graphene-PR was transferred onto the surface of clean SI-4H-SiC substrate. The substrate was baked at a temperature of $110\ ^{\circ}C$ in order to provide better adhesion of graphene layer to the surface of the substrate. As for the last step, PR was removed in hot acetone to leave the graphene layer alone on the SI-4H-SiC substrate.

3.2. Deposition of Cr/Au Contacts for Optoelectronic Measurements

After the growth of the samples, the metallic electrodes were thermally deposited for the electronic characterization measurements. For our thermal evaporation system, we designed a sample holder and hard masks to evaporate metallic electrodes in proper geometries. Holder and hard masks were designed in AutoCAD and were manifactured by Sparks Technologies Turkey by laser cutting system with the high precision of $5\ \mu m$. In our laboratory, our sample geometry standarts are $10 \times 10\ mm^2$. Therefore, the designed holder has 32 cells with a $10.1 \times 10.1\ mm^2$ sized (Figure 3.4).)

The holder consists of two $300\ \mu m$ thick stainless steel sheet: one of them has $9.5 \times 9.5\ mm^2$ sized cells and other one has $10.1 \times 10.1\ mm^2$ sized cells. Since our evaporation boats are below the substrates, we need to avoid substrates from falling. Combining the $9.5 \times 9.5\ mm^2$ cell sized holder with the $10.1 \times 10.1\ mm^2$ cell sized holder helps to secure the samples from falling down. Both holders were manifactured with a precision of $10\ \mu m$. Our hard masks have the thickness of $150\ \mu m$ and the dimensions of $10 \times 10\ mm^2$ squares. After the desired hard masks are put into the sample cells, the samples are ready to put on the hard masks. We have $150\ \mu m$ step to avoid the sample sliding during the evaporation process. Although $80\ nm$ gold was sufficent to fabricate metallic electrodes, the inert structure of gold decreases the sticking quality on the surface. This

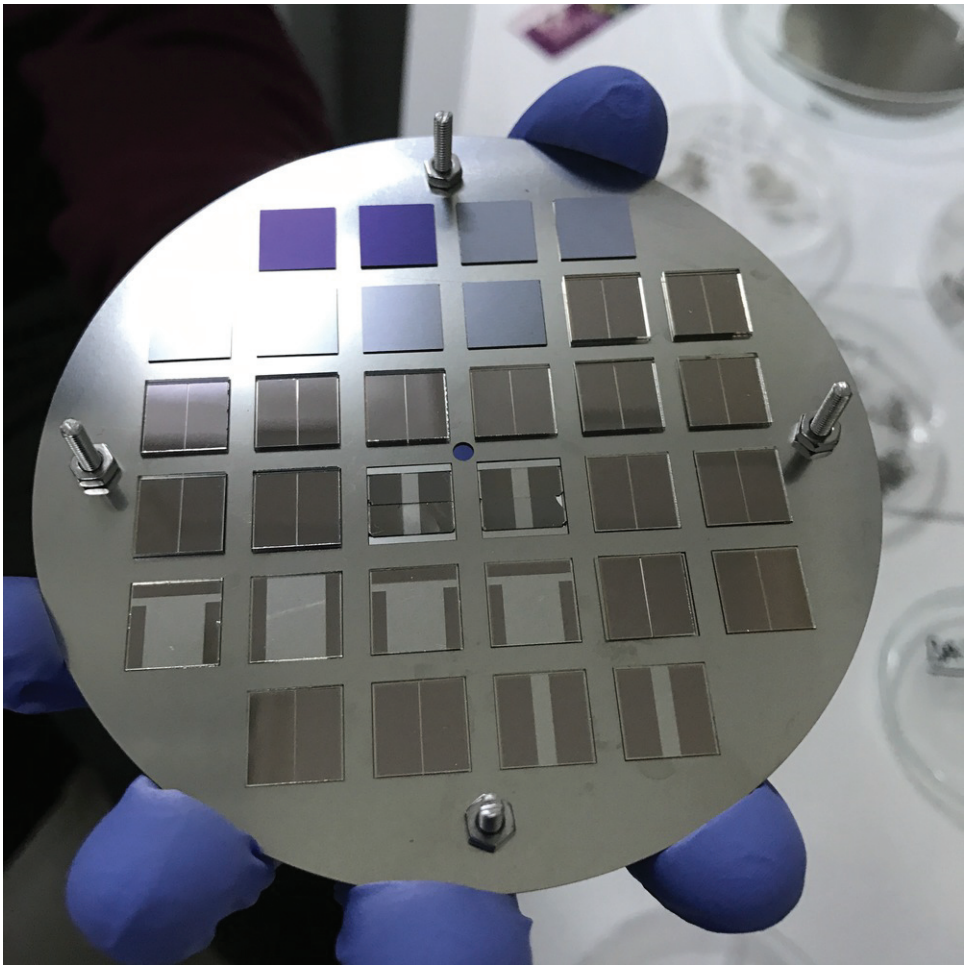

Figure 3.4. The sample holder of Thermal Evaporation System in Quantum Devices Laboratory. It has the diameter of 4″, and 32 cells for loading $10 \times 10\ mm^2$ substrates. Hard masks can be seen as light gray, coated chromium contacts can be seen as dark gray.

results in easy scratches while wire bonding. Therefore, $5\ nm$ chromium was evaporated before the vaporization of gold to increase the stickiness of the gold.

3.3. SiO_2 Encapsulation of Graphene

Two different encapsulation method is used for the passivation of the graphene layers. Thermal evaporation is a low-cost evaporation method, whereas the Pulsed Electron Deposition is a plasma based evaporation method.

3.3.1. Thermal Encapsulation

Figure 3.5. (a) The NVTH-350 Thermal Evaporation System in Quantum Device Laboratory. (b) (1) Radiative heater, (2) Quartz crystal monitor for precise thickness measurements, (3) sample holder, (4) Four boats (left-top: SiO_2, right-top: Al, left-bottom: Cr, right-bottom: Au) are placed in the high vacuum chamber. The system allows to evaporate different materials without breaking the vacuum, which is essential for materials convenient to oxidation.

Thermal evaporation is one of the easiest deposition method to obtain high quality metallic electrodes. It is simply based on heating a Tungsten (W) boat by Joule heating method. Evaporation material is thermally contacted with W, so when W is heated, source is heated up, too. The pebble like SiO_2 pellets were used for the vaporization. Thus, a W basket was utilized in order to fill pellets easily for the evaporation. SiO_2 sublimates at a melting degree of $1610\ ^{\circ}C$. Before sublimation of the SiO_2, the degass procedure was performed to enhance the quality of the encapsulated thin film. Degass occured after applied power of $5\ W$ to the basket. In our system, the sublimation temperatures were achieved after $5\ V$ potential difference was driven between the contacts of W basket. Meanwhile, the total power that was measured $240\ W$. The thickness of the deposited SiO_2 was $100\ nm$.

3.3.2. PED Encapsulation

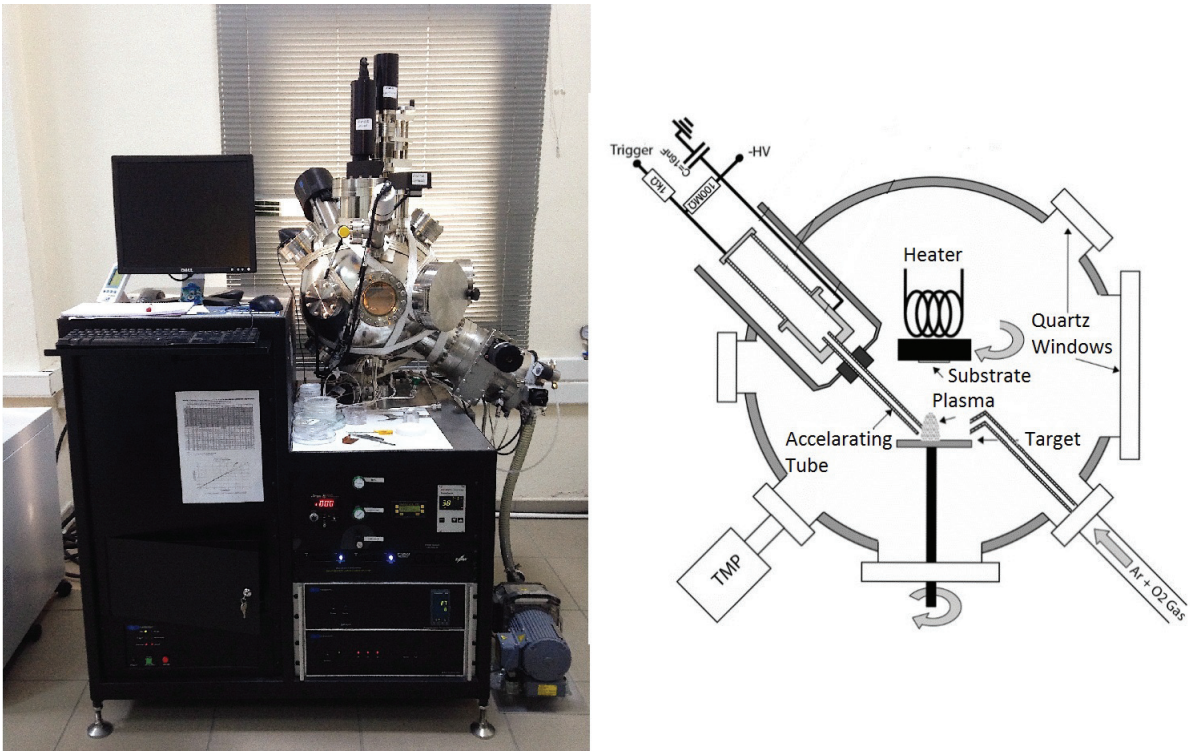

Figure 3.6. (a) The Neocera Pulsed Electron Deposition System in Quantum Devices Laboratory. (b) The sketch of the chamber: TMP is used for fabrication of samples in high vacuum conditions. Gas flows are controlled by MKS precise flow meters. (Source: Tricot et al. (2008))

PED is a gas assisted plasma technique which is based on the ablation of the target by high power pulsed electron beam. The high energetic electron beam is focused onto the target and the interaction of the beam with the assisted gas is provided. This interaction results in cracking of the assisted gas and leads to generation of plasma on the target with a penetration depth of around $1\ \mu m$. Plasma gives rise to a rapid evaporation of the target material. Ablation is localized by the focused electron beam and thus the stoichiometry of the target is preserved (Figure 3.6). PED is the one of the novel methods for deposition of thin films, especially metal-oxide based semiconductors. Owing to their very high forbidden gap energy, it is infeasible to ablate wide band gap semiconductors or insulators with a pulsed laser beam. The energy of the pulsed electron beam can be increased up to $18\ kV$ in PED system. Therefore, it becomes possible to ablate the wide

gap semiconductors or high-k dielectrics. The encapsulated SiO_2 was grown $100\ nm$ under $5.5\ mTorr$ O_2 pressure with $9.5\ kV$ discharge voltage.

3.4. Chip Carriers and Wire Bonding

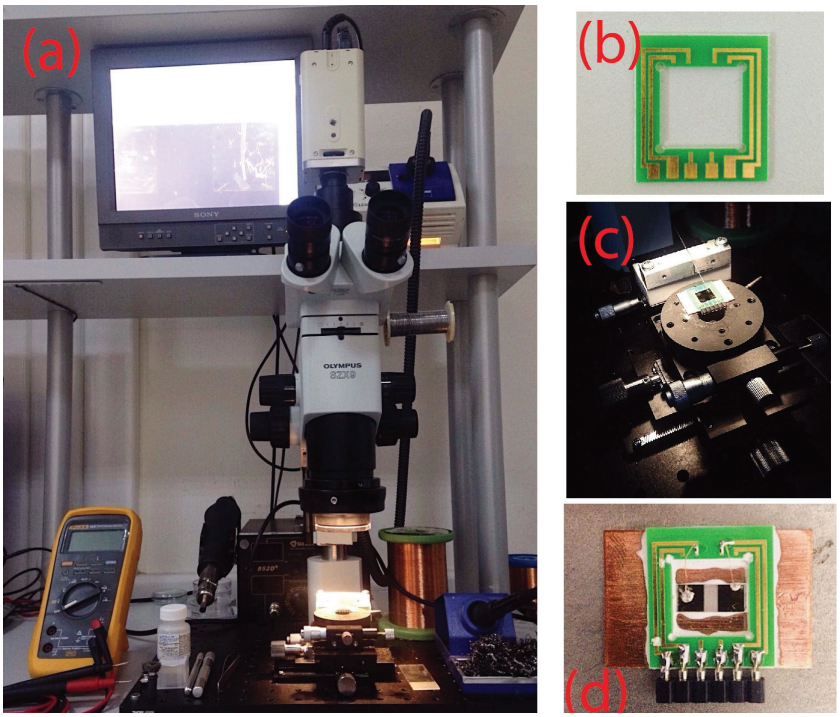

Figure 3.7. (a) Lab-built wire bonder. Cu wires is used to bond sample′s metallic electrode (Al, Au) with chip carrier Au guide in order to get electrically contacted with sample box. (b) The chip carrier with gold plated paths. The example for (c) during the wire bonding and (d) after bonding.

After the deposition of metallic electrodes, the next step was to stick the sample onto the sample holder and then on the chip carrier. Ceramic adhesive epoxy was used in both steps. Afterwards, sample electrodes were bonded to the gold plated chip carrier paths to connect the pins of the cryostat. For the bonding processes, lab-built wire bonding station was used and can be seen in Figure 3.7. $80\ \mu m$ copper wires were used for connection while indium was utilized for connective material.

3.5. Electronic and Optoelectronic Characterization Setups

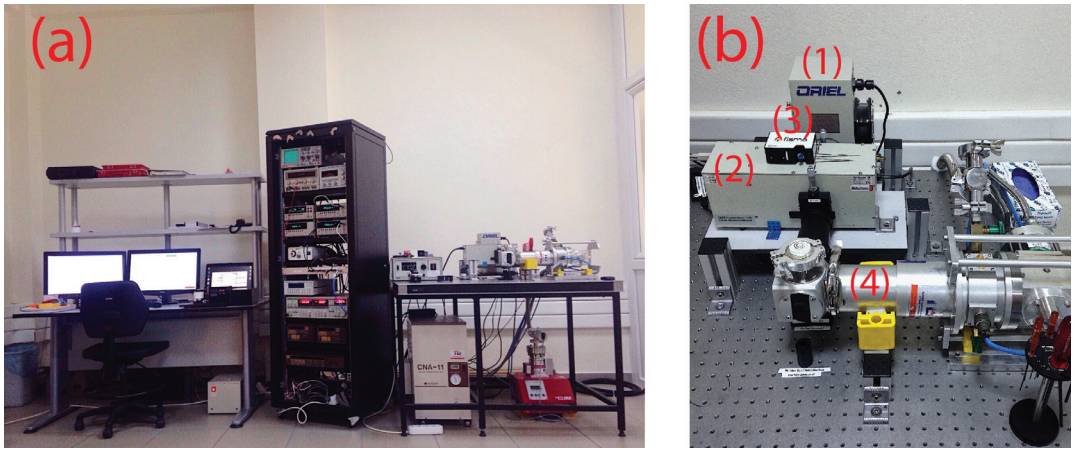

Figure 3.8. (a) Electronic and optoelectronic characterization units in Quantum Device Laboratory at IZTECH. (b) The photocurrent spectroscopy setup.

With our electronic and optoelectronic characterization units, it is possible to perform AC/DC resistance and conductance measurements as a function of temperature, wavelength and pressure. Electronic and optoelectronic characterizations were performed using rack unit including Keithley 2400-236 Source-Measure Units as voltage and current sources, Keithley 6485 Picoammeter for the current measurements, SRS830 Lock-in Amplifier for detection of AC voltage and current, Keithley 230 as voltage source, Keithley 2182a Nanovoltmeter for the precise nanovolt measurements, Lakeshore 330 Temperature Controller for cryogenic applications and GW-Instek power supply for rough voltage source, a Pfeiffer High Cube TMP for the high vacuum applications, respectively.

3.5.1. Photocurrent Spectroscopy Setup

The PS setup (Figure 3.8 (b)) consists of a quartz tungsten halogen lamp (1), a high resolution monochromator (2), a spectrometer (3) and a power detector to measure light power output. PS setup allows us to measure the illumination power dependent transient photocurrent and wavelength dependent responsivity measurements of the photodiodes/photodetector devices especially whose are produced in Pulsed Electron Deposition system in Quantum Device Laboratory. PS setup is integrated to a $5\ K$ to $300\ K$

closed loop cryostat (Figure 3.8 (4)) that provides temperature dependent measurements under low 10^{-5} mbar vacuum range. The entire setup is PC controlled and interfaced with GPIB card and connectors. Quartz tungsten halogen lamp has a broadband spectrum from near UV to near IR as similar to solar spectrum. With a monochromator, it is possible to monochrome the wide band spectrum into the selected wavelength. In our laboratory Oriel Cornerstone CS130 High Resolution monochromator is used for narrowing the broad spectrum. The monochromator has a operation range of $200\ nm$ to $1200\ nm$ (can be sweeped by $0.1\ nm$ interval) with two slits at the in and out ports. Moreover, it has two different high resolution gratings to intensify efficiency while narrowing the spectral distribution. The first grating is specifically enhanced between $200\ nm$ and $515\ nm$, whereas the second grating is improved to operate between $515\ nm$ to $1200\ nm$. It is become more of an issue while working with the second grating. Halogen lamp has its most intense output in visible region. Therefore, the second harmonics of the beam can be introduced. In order to supress this unwanted harmonics, a long pass filter which passes $515\ nm$ and above is used. The full width at half maximum (FWHM) of the monochromed beam can be arranged by adjusting the entry and exit slits. However, closing the slits for narrowing the FWHM results in a drop in intensity. This adjustment must be optimized for every sample for choosing the proper wavelength interval.

Ocean Optics Flame Spectrometer is used for optimizing the FWHM precisely. The spectrometer works in the range of $200\ nm$ and $1000\ nm$ with minimum $1\ ms$ shutter time. It can be used either its own interface or MATLAB. However, spectrometer could not measure the power output after proper adjustment of the slits. Thus, the commercial photodetector (FDS10x10 Si photodiode which is purchased from Thorlabs.) is used for measuring the power output in units of watt after calibrating the FWHM. The wavelength dependent responsivity values of the photodetector is calibrated by Thorlabs. With a proper integrated circuit, it is possible to measure current increment under monochromatic light, hence the power output from the relation of $R = A/W$. Thus, the wavelength dependent current alteration per watt can be measured and responsivity of the manifactured device can be deduced with the same responsivity-current-watt relation.

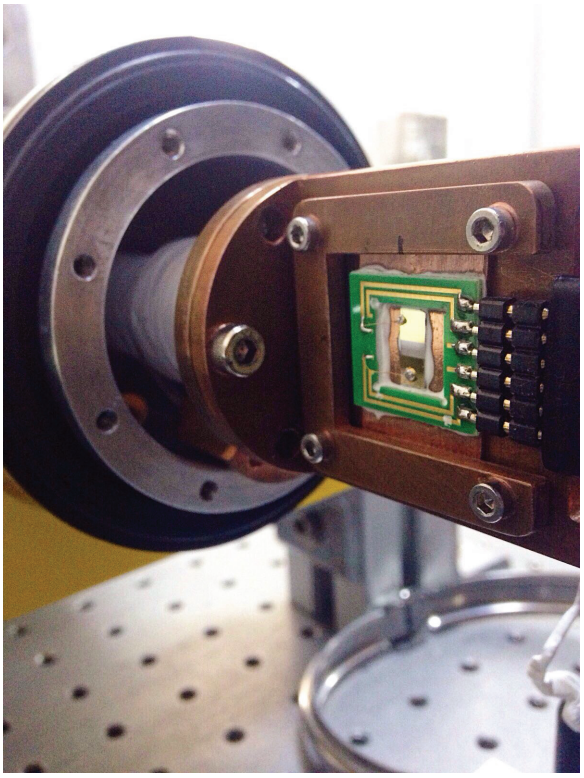

Figure 3.9. Picture of the sample after loaded onto sample holder of cryostat.

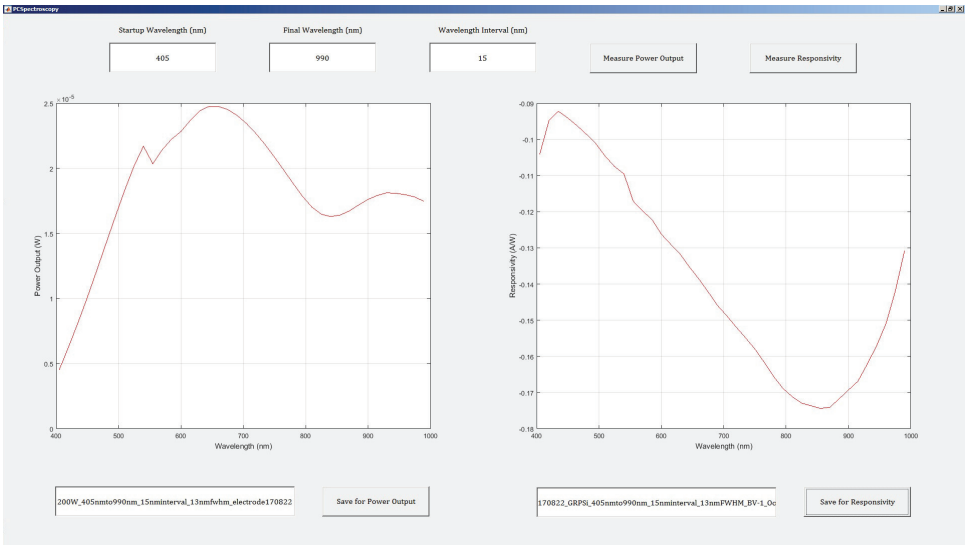

Figure 3.10. The user interface of PS Setup, which is written in MATLAB.

3.5.2. Probe Station

One of the most fundamental electronic transport characteristics of thin films is the mobility. Mobility is not a directly measurable quantity (except Quantum Hall Effect measurements), so one needs to combine the resistivity and classical Hall effect measurements to acquire the mobility of the samples.

$$\sigma = ne\mu \tag{3.1}$$

In order to perform resistivity and Hall effect measurements, 4-Terminal (4W) contacts must be deposited in the geometry of van der Pauw structure. Therefore, we built a probe station which is named as "Black Box" in our laboratory (Figure 3.11 (a)) including the proper orientation of the pins for van der Pauw geometry. With its source (Keithley 6220 Precision Current Source) and measurement (Keithley 2000 Digital Multimeter) units, it is allowed to measure the sheet resistance and sheet density of the thin films, in addition to conduct 2-Terminal (2W) IV measurements.

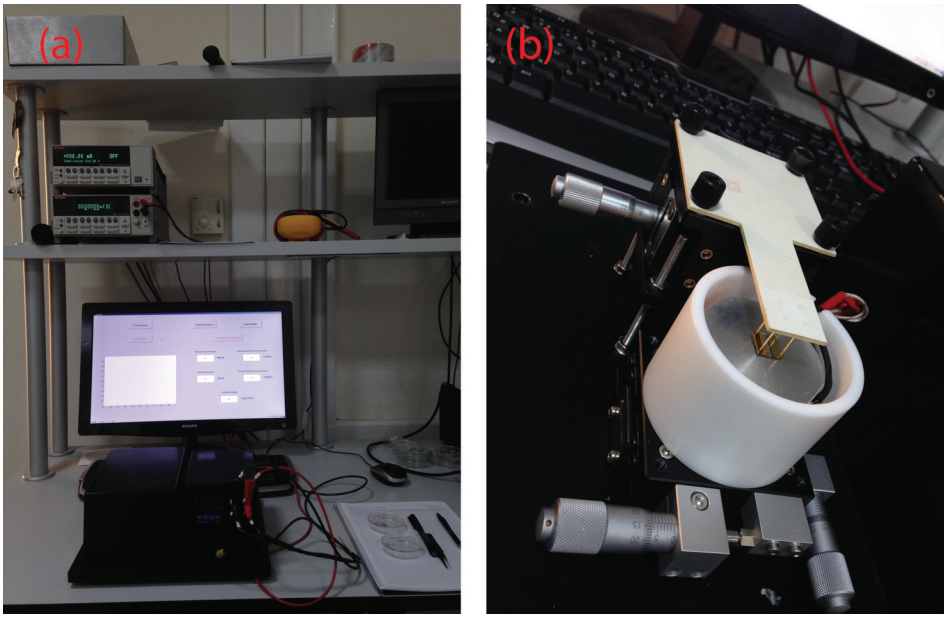

Figure 3.11. (a) The probe station setup. (b) The probes which are connected independently of each other, have been mounted to a z-axis stage to approach sample surface with a precision of micrometer. The sample holder has movement opportunity in x-axis and y-axis to arrange ideal contact configuration.

Probe station has also its own PC and interfaces which was written in MATLAB. The sample mount of the probe station also provided us to sweep the temperature between $300\ K$ to $450\ K$. The mathematical formulation and the progression between the steps are based on "National Institute of Standards and Technologies: Resistivity and Hall Effect Measurements Techniques".

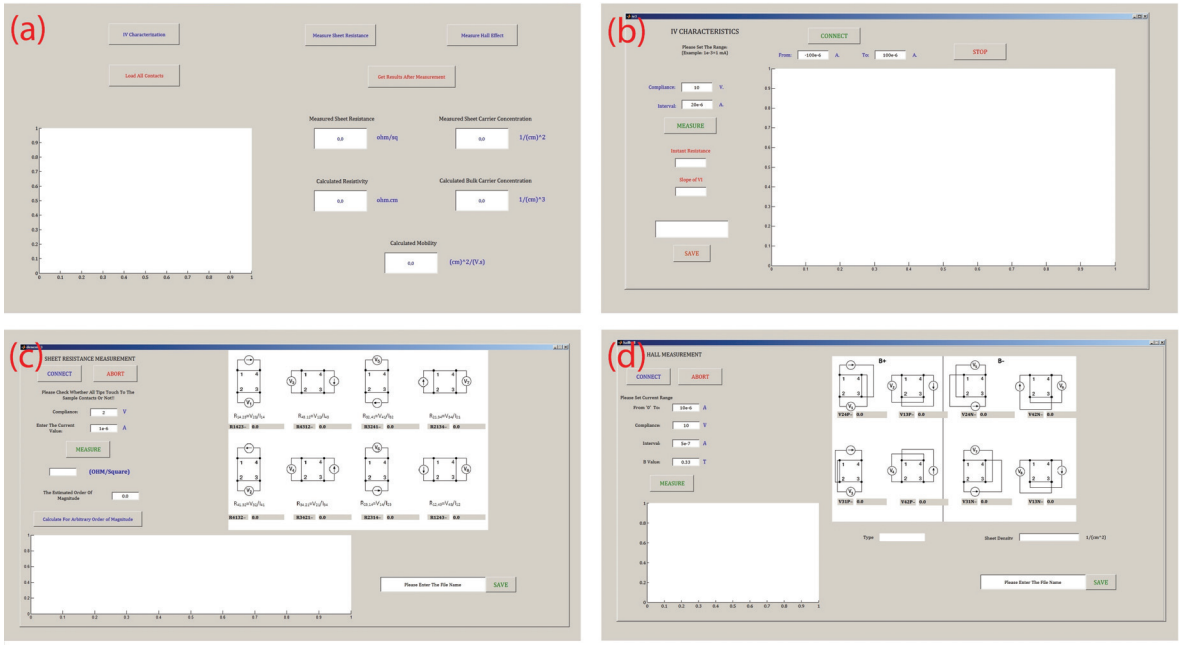

Figure 3.12. The user interface of Probe Station. (a) The main program, (b) 2W IV characterization program, (c) 4W sheet resistance measurement program, (d) 4W classical Hall measurement program.

Main program consist of three different programs (Figure 3.12 (a)). Firstly, we conduct 2W IV characterization (Figure 3.12 (b)) to check the ohmic contact quality of the sample with the deposited metallic electrodes. In order to measure the mobility, all electrodes must be ohmic contact. Afterwards, we proceed with the sheet resistance program (Figure 3.12 (c)). All contact configurations is guided by the programme itself. Next we get four horizontal four vertical resistance values and the sheet resistance is calculated. We put the neodymium magnet and carry on with the classical Hall effect measurement (Figure 3.12 (d)). After Hall effect measurements we return back to main program to deduct the mobility with the measured values of sheet resistance and sheet carrier density.

One of the key properties of our Probe Station which is shown in Figure 3.11 (b), is to measure 2W and 4W characteristics of samples without any destruction. This helps

us to get different measurements from the same sample, such as Raman Spectroscopy or XRD measurements. Moreover, each probe has their own spring to protect sample against the extra pressure and scratching the metallic electrodes while approaching to the surface.

CHAPTER 4

TPS MEASUREMENTS

4.1. Before SiO_2 Encapsulation

Pirkle et al. (2011) and Suk et al. (2013) showed that graphene layers grown by chemical vapor deposition (CVDG) has strong p-type carrier density while the epitaxial graphene (EG) layers produced on the Si-face surface of SiC substrate exhibits an inherent n-type conductivity (Eriksson et al. (2012), Kopylov et al. (2010) and Sidorov et al. (2012)). Therefore, in order to make a viable comparison between two different charge carrier types for the same material, we used both monolayer CVDG and EG that were either transferred or directly grown on SI-SiC substrates.

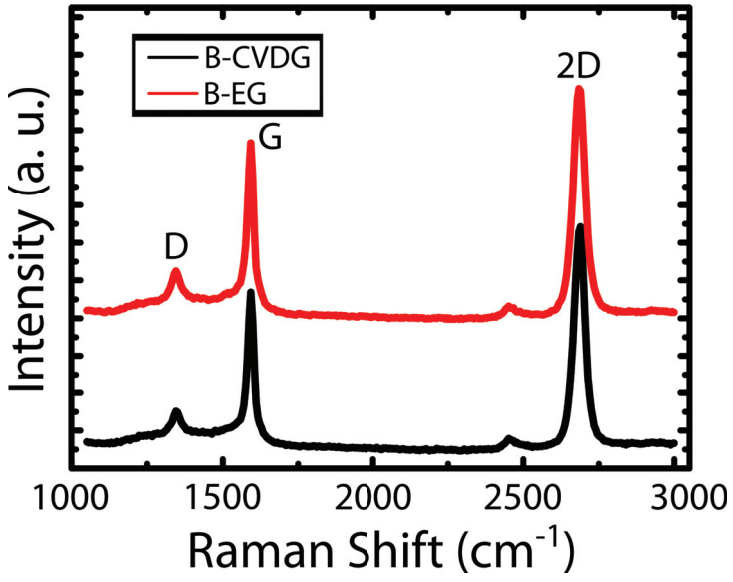

Figure 4.1. Raman Spectroscopy results of B-CVDG and B-EG.

Raman Spectroscopy was performed to identify number of graphene layers, quality and continuity of graphene. Raman spectra indicate typical appearance of SiC background attenuated (Shivaraman et al. (2009), Kus et al. (2015)) graphene on SiC substrate

including D (1344 cm^{-1}), G (1589 cm^{-1}) and 2D bands (2690 cm^{-1}), respectively (see Figure 4.1). The G band is the first Raman peak related to C-C stretching of sp^2 carbon. The 2D band is the second order graphene peak and the D band provides information about amount of disorder in graphene. Intensity ratios of G/2D and D/G have been utilized to determine the number of graphene layers and defect content of graphene. While $I_{G/2D}$ and $I_{D/G}$ were about 0.6 and 0.13 for epitaxial graphene, The CVD graphene of $I_{G/2D}$ and $I_{D/G}$ was found to be 0.6 and 0.13, respectively, resulting the presence of high quality monolayer graphene on SI 4H-SiC substrate (Aydin et al. (2018), Lin et al. (2015)).

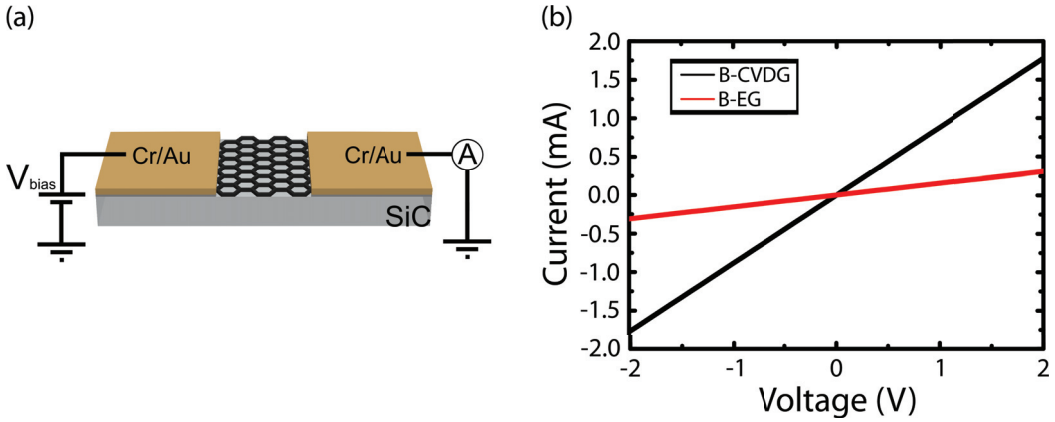

Figure 4.2. (a) The device schematics (not to scale). (b) The IV characteristics of bare CVDG and bare EG.

IV measurements were conducted for both CVDG and EG and the obtained results are compared in Figure 4.2 (b). The initial resistance of bare CVDG (B-CVDG) was measured as $1.1\ k\Omega$ and the initial resistance of bare EG (B-EG) is $6.5\ k\Omega$. The adsorbates like O_2 and H_2O in air serve as surface states and hence the adsorption/desorption of these molecules drastically alter the electronic transport characteristics via charge transfer doping effect. Firstly, samples were left in ambient and the resistance alteration was measured. The resistance of B-CVDG was decreased, while the resistance of B-EG was increased (Figure 4.3 (a)). As discussed in Chapter 2, adsorption could be physical or chemical. So, the adsorption type must be distinguished from each other. Vacuum measurements are carried out in order to investigate the physisorbed adsorbates. The results are shown in Figure 4.3 (b). Physisorption dynamics can be easily manipulated in room temperature, because of the binding energy of physisorbed adsorbates are comparable with the thermal energy at room temperature ($k_bT = 25.4\ meV$). The physisorption contribution to the electronic instability of graphene is about $2-3\ \%$. This results are similar

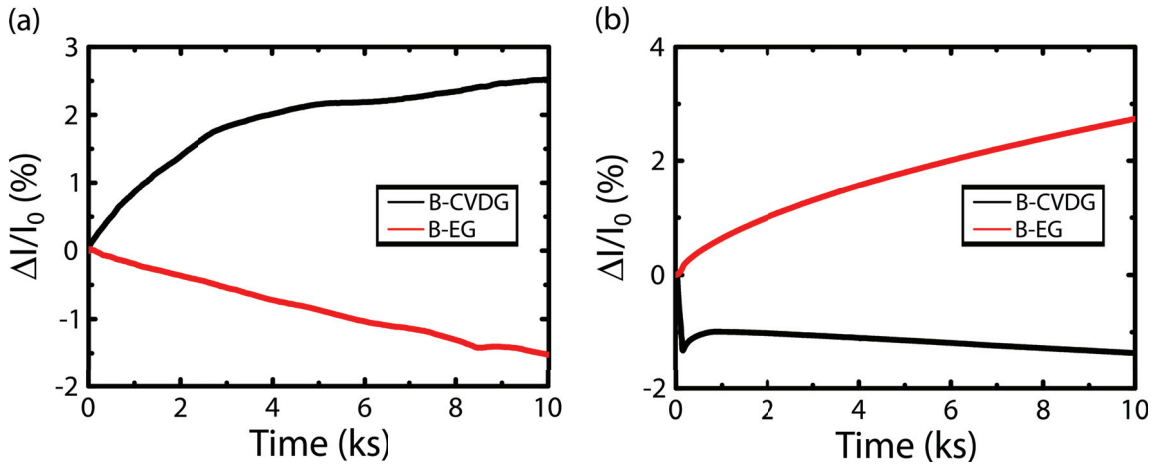

Figure 4.3. (a) The time dependent resistance variations of B-CVDG and B-EG under atmospheric gases. (b) Resistance alteration of B-CVDG and B-EG as a function of time under vacuum.

to the conductivity variation results of Yang and Murali (2011).

Although there are a variety of studies regarding the adsorption/desorption of O_2 and H_2O molecules by graphene, there are no TPS measurements conducted to get a deep insight into the adsorption/desorption induced variations in the resistivity of graphene but with two different charge carrier types. To promote desorption of adsorbates which were already stuck on graphene in air, the samples were exposed to UV light for a period of $5\ ks$ under high vacuum conditions. The irradiation wavelength is specifically selected to be $254\ nm$ since it is energetically sufficient enough to desorb O_2 and H_2O molecules (Ryu et al. (2010), Danielson (1987)) from graphene layer and at the same time to generate excitons in the depletion region of underlying SiC crystal due to its wide band gap ($E_g = 3.2\ eV$). Figure 4.4 shows that as the UV light desorbs the adsorbates, the current of B-CVDG decreases monotonously in contrast to the increase of the current for B-EG. This opposite behavior seen in the current characteristics suggests that the charge carrier types in these two graphene layers are indeed different from each other. After $5\ ks$ period of UV light illumination, the changes in the current of B-CVDG and B-EG were measured as high as $45\ \%$ and $110\ \%$, respectively. When the UV light is turned off, the adsorbates with lower partial pressure at middle 10^{-5} mbar vacuum range tend to stick back onto the graphene layer and hence give rise to a slight variation in the final resistance level of the samples. We have found that even after $5\ ks$ duration, the resistance of the sample

could not reach to its initial value measured before the UV light illumination. Due to the negligible alterations in the physisorption compared to chemisorption, we focused on the effect of chemisorbed adsorbates.

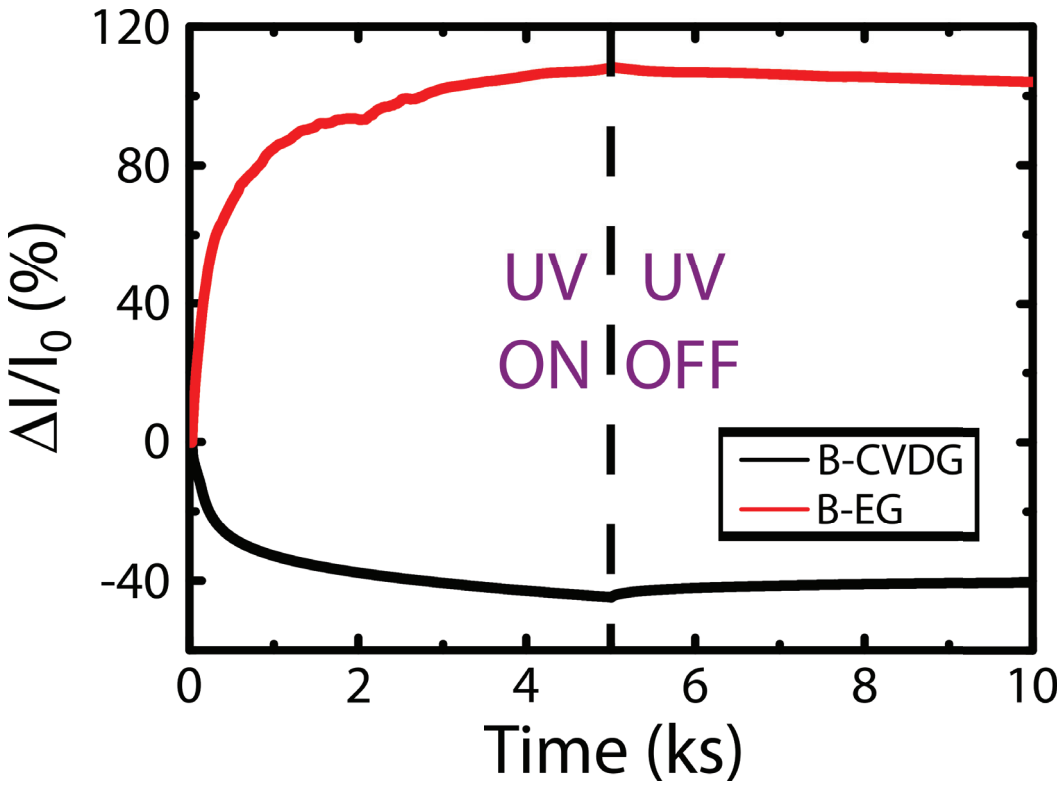

Figure 4.4. The $5\ ks$ one cycle transient photocurrent spectrum of B-CVDG and B-EG.

The TPS measurements applied for short periods and a couple of cycles can be more useful to get a deep insight into the distinct behaviors behind above mentioned current characteristics of the samples. For the TPS measurements, we set the shutter period to $30\ s$ only for three cycles. Prior to the experiments, all the samples were exposed to UV light in vacuum for $10\ ks$ duration to make sure that the adsorbates are removed in a large extent from graphene layer. For B-CVDG sample, a sudden drop in the current is observed within a second when the shutter is closed (Figure 4.5 (a)). Then in a couple of seconds, the adsorbates with a lower partial pressure in vacuum (middle 10^{-5} mbar) are adsorbed by the graphene layer over time resulting in an exponential growth of the current. Under the UV light illumination, a sharp increment in the current occurred also within a second, which is followed by a rapid exponential decay. From the literature, we are aware of the fact that the adsorption of O_2 and/or H_2O molecules dopes graphene with holes. This explains well the time dependent but slow variation of the current in

our B-CVDG sample when the UV light is either turned on or off. Since the adsorption rate with the measured time constant of $\tau_{ad} = 21.7\ s$ is smaller than the desorption rate $tau_{des} = 13.2\ s$), an upward trend was observed in the overall current variation within a couple of on/off cycles.

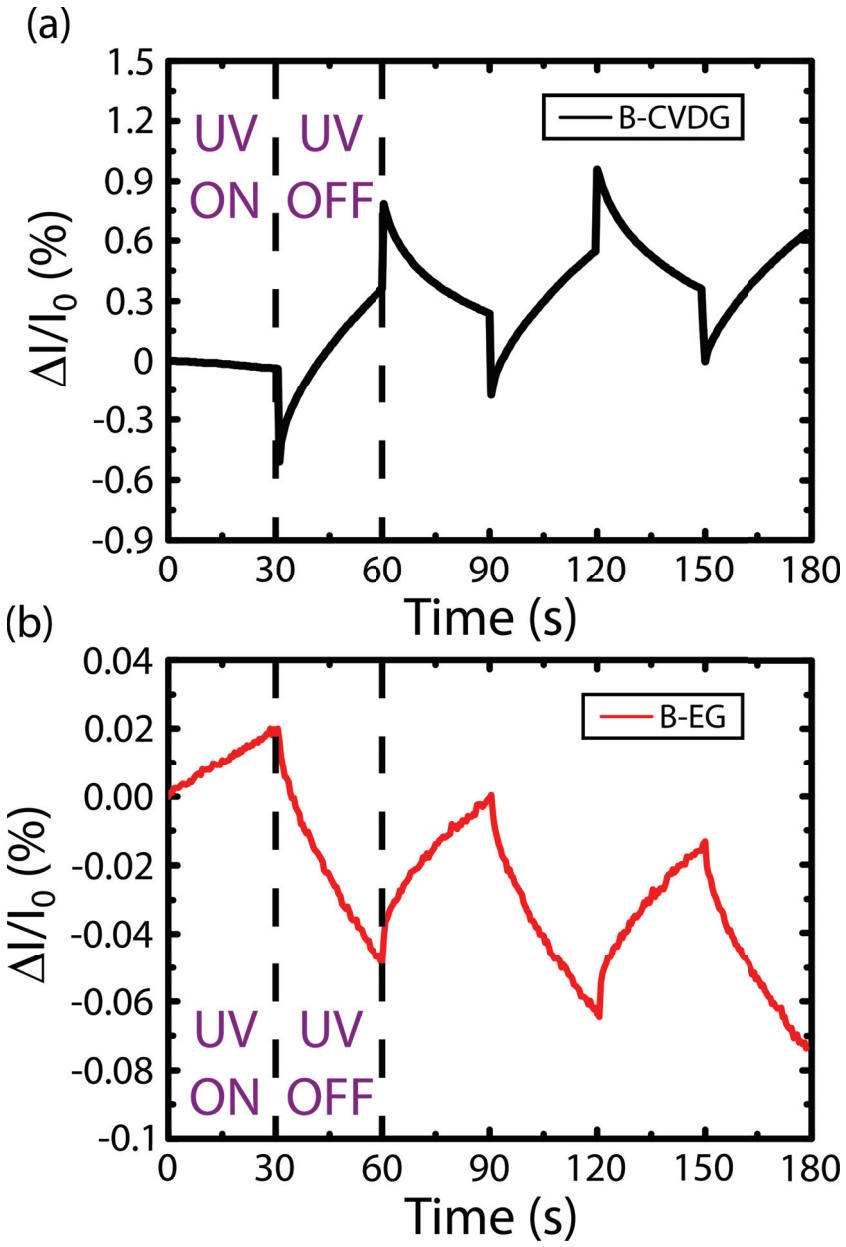

Figure 4.5. The $30\ s$ three cycle transient photocurrent spectrum of B-CVDG and B-EG.

For B-EG, a relatively weak but fast decrement in the current is followed by an exponential decay when the shutter is closed (Figure 4.5 (b)). Similar to that observed in B-CVDG, we measured a sudden rise in the current within a second after the shutter

is opened. However, following the first steep rise, the current raised exponentially as a function of time unlike the exponential decay of the current measured for B-CVDG. This observed behavior in the current variation for B-EG cannot be explained simply by the adsorbate induced hole doping process. The measured TPS characteristics of our B-EG is similar to that of n-type metal-oxide based semiconductors like ZnO thin films, which is discussed in Chapter 1.6. For example, the adsorbates that were stuck on the surface of n-type ZnO film trap the free electrons and thus lead to a drastic drop in the current under atmospheric conditions. In analogous, as the UV light desorbs the adsorbates from B-EG layer, the trapped electrons are released over time and therefore give rise to an exponential increment in the current. For B-EG, the adsorption rate with the measured time constant of $\tau_{ad} = 27.5\ s$ is also smaller than the desorption rate ($\tau_{des} = 17.9\ s$). However, unlike B-CVDG, the difference between the adsorption rate and desorption rate for B-EG causes a downward trend in the overall current variation within a couple of on/off cycles.

4.2. After SiO_2 Encapsulation

Two different encapsulation method is used for the passivation of the graphene layers. Thermal evaporation is a low-cost evaporation method, whereas the Pulsed Electron Deposition is a plasma based evaporation method.

4.2.1. Encapsulation of Graphene Layers by Thermal Grown SiO_2

Interactions of graphene layers with the atmospheric gases are investigated in the manner of physisorption and chemisorption. These adsorbates cause electrical instabilities, exclusively in optoelectronic applications. Surface passivation with a dielectric is one of the fundamental method to suppress the adsorbate effects. Thus, $100\ nm$ SiO_2 is grown by thermal evaporation to encapsulate graphene layers.

The IV characteristics of thermally encapsulated CVDG (TE-CVDG) and EG (TE-EG) are shown in Figure 4.6 (b) and (c), respectively. No significant change in the measured resistance is observed after thermal encapsulation. The resistance of B-CVDG is increased up to $1.64\ k\Omega$, whereas the resistance of B-EG is decreased down to $4.93\ k\Omega$. The change in the resistance for both samples are still in the same order of magnitude compared to bare samples after the thermal encapsulation.

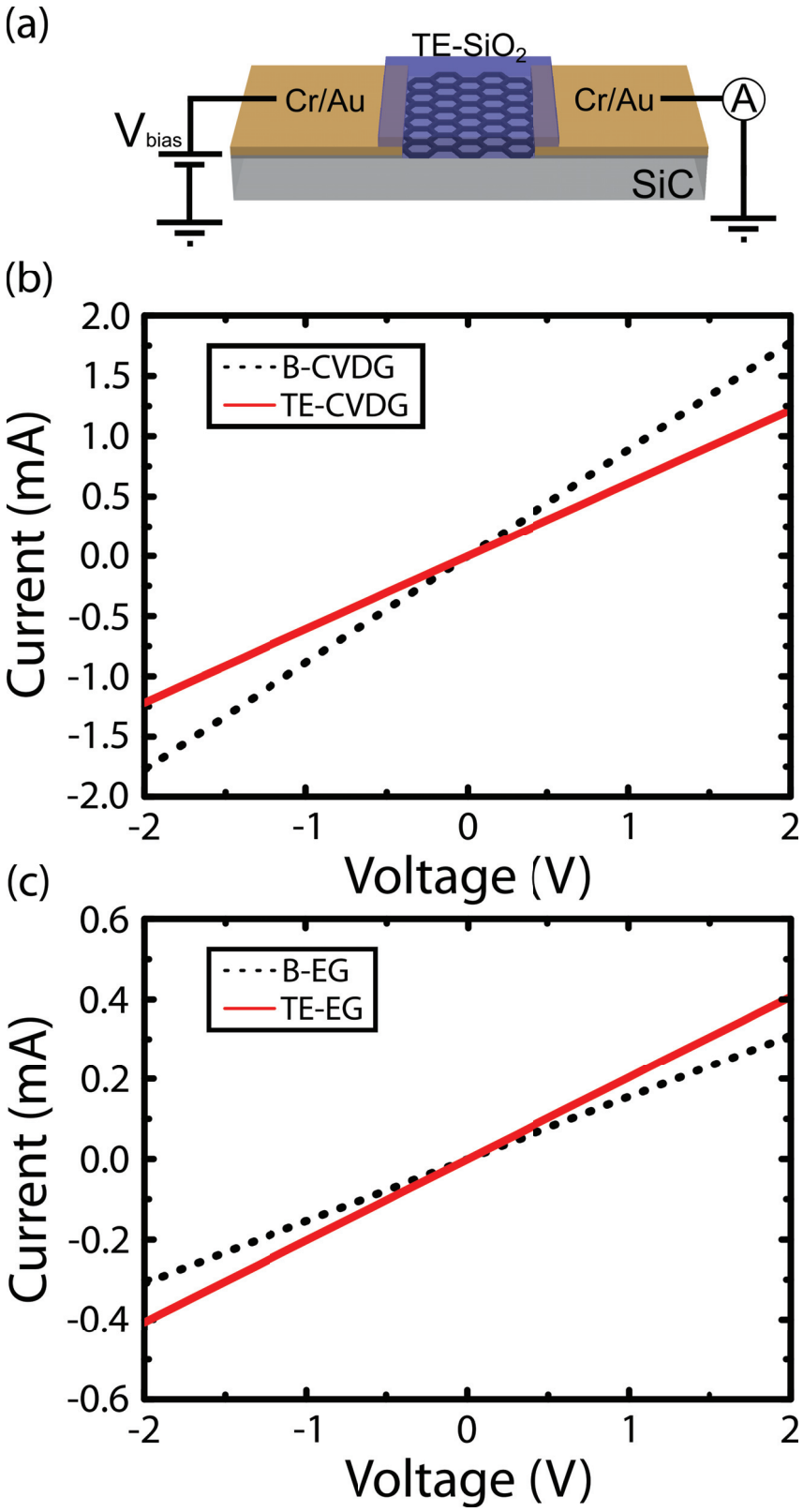

Figure 4.6. (a) Device schematics after thermal encapsulation. The IV characteristics of (b) CVDG and (c) EG before and after thermal encapsulation.

The vacuum dependent resistance alterations of TE-CVDG and TE-EG are shown in Figure 4.7 (a) and (b), respectively. For TE-CVDG and TE-EG, the physisorption is seemed to be suppressed by around $50\ \%$ as compared with the B-CVDG and B-EG, but not completely eliminated after $10\ ks$.

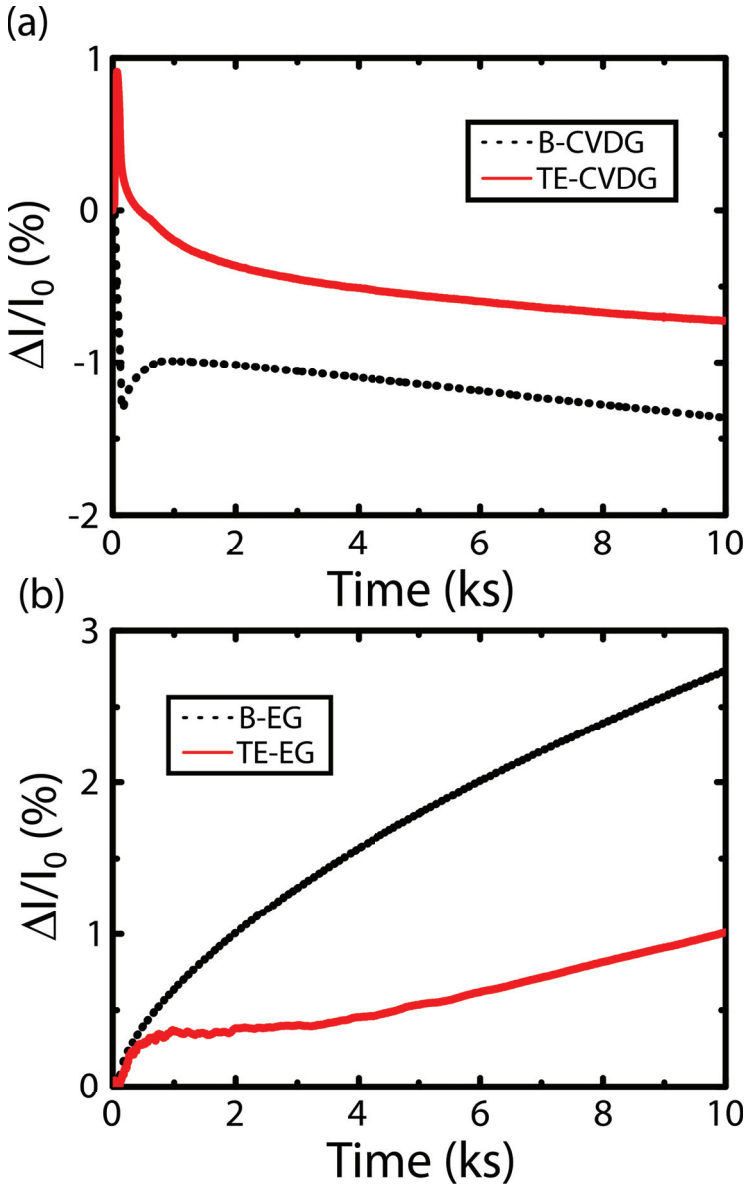

Figure 4.7. The time dependent resistance variations of (a) CVDG and (b) EG under vacuum before and after thermal encapsulation.

One cycle with a period of $5\ ks$ TPS measurements are conducted in order to investigate the interaction between chemisorbed adsorbates and the graphene layers after the thermal encapsulation. As shown in Figure 4.8 (a), the current alteration of TE-CVDG

is decreased from $45\ \%$ to about $30\ \%$ after $5\ ks$. TE-CVDG could not be recovered to its initial conditions. This is the proof of the chemisorption: TE-CVDG layer is still chemically interacting with the adsorbates. Same behavior is observed for EG after thermal encapsulation. The measured current of TE-EG alters around $50\ \%$ under the UV illumination, but the total variation is around $2\ \%$ after the UV light is off (Figure 4.8 (b)). EG layer is also chemisorbed adsorbates from the atmosphere, when it exposed to ambient after the SiO_2 encapsulation in thermal evaporator. These results ensue that the chemisorption could not be supressed with the thermal encapsulation for both types of graphene.

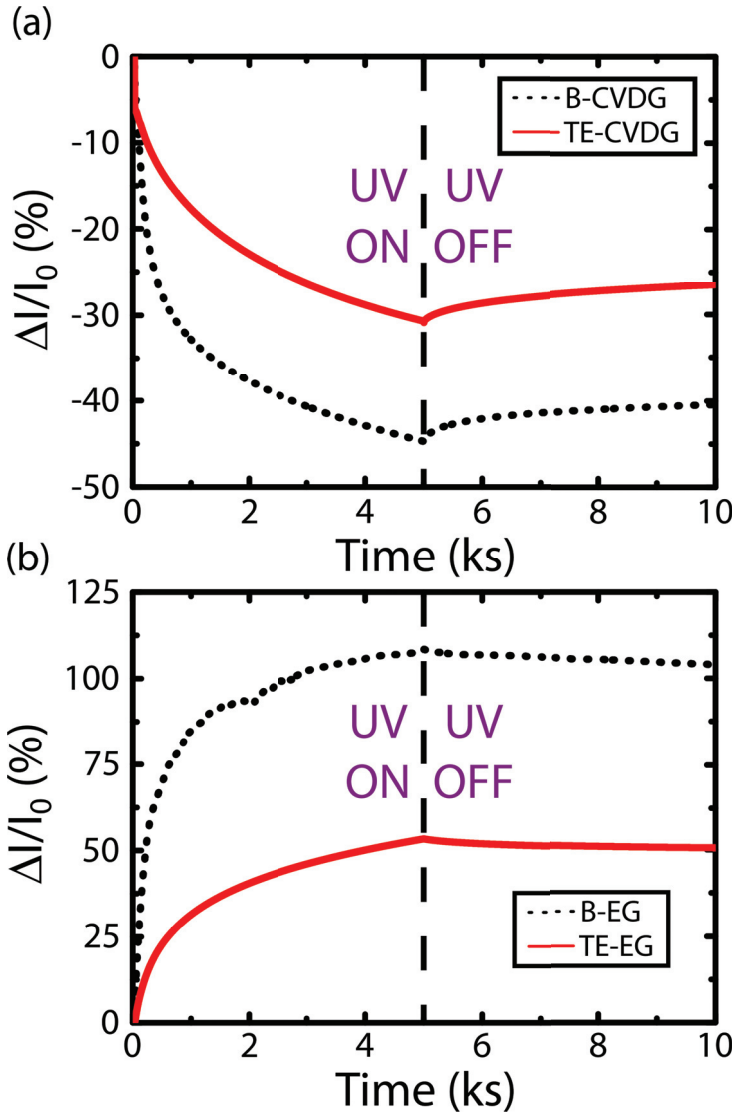

Figure 4.8. The $5\ ks$ one cycle transient photocurrent spectrum of (a) CVDG and (b) EG before and after thermal encapsulation.

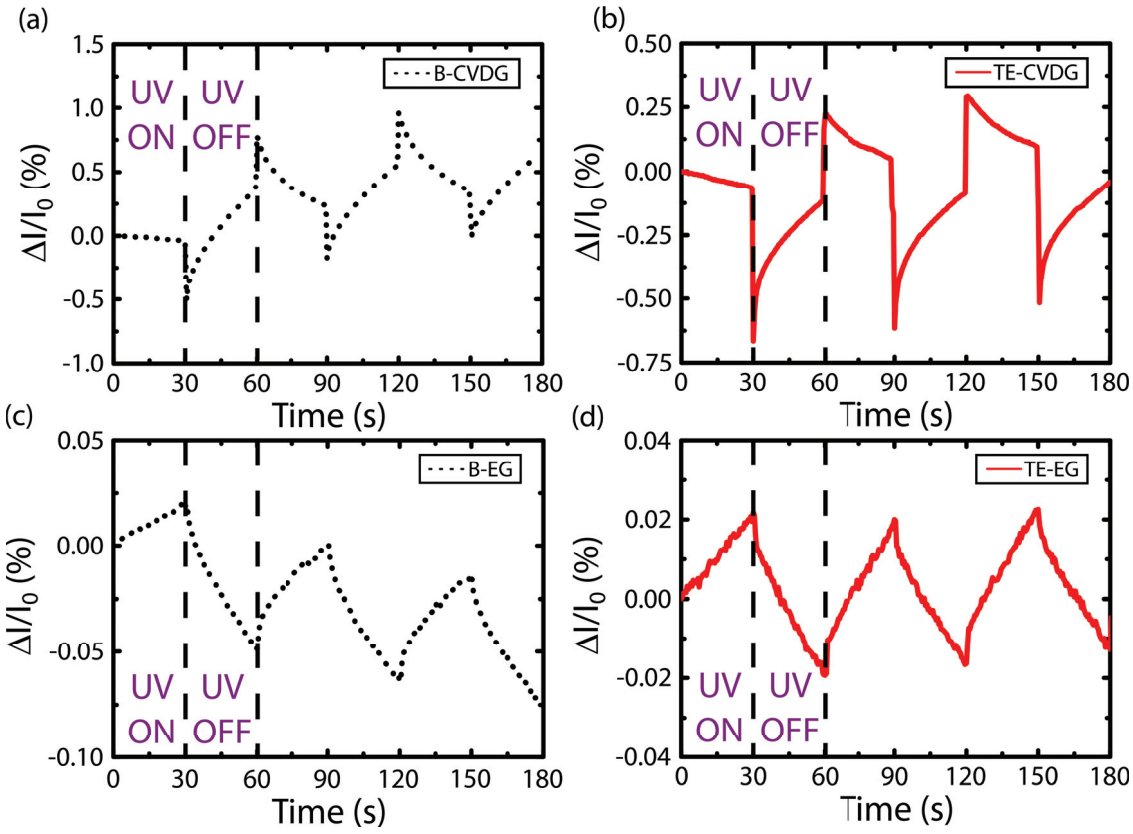

Figure 4.9. The 30 s three cycle transient photocurrent spectrum of (a) B-CVDG, (b) TE-CVDG, (c) B-EG, and (d) TE-EG.

We deeply investigated the chemisorption of adsorbates by shortening the period and increasing the cycles of TPS measurements. Before and after thermally encapsulated CVDG results are indicated in Figure 4.9 (a) and (b). Adsorption and desorption rates are balanced in TE-CVDG, unlikely in B-CVDG. This ensues the stabilization of observed upward trend the B-CVDG after encapsulation. Under UV illumination, the photogenerated carrier alteration is comparable to time dependent adsorption variation. In Figure 4.9 (c) and (d), the current alteration of B-EG and TE-EG layers are depicted. After encapsulation the contribution of photogenerated carriers are slightly increased similar to the TE-CVDG. The downward trend of B-EG is also balanced. However, rectified and sharp transitions could still not be observed. Thus, the passivation quality of the graphene layers by thermal evaporation of SiO_2 is inadequate to optoelectronically stabilize the samples.

4.2.2. Encapsulation of Graphene Layers by PED Grown SiO_2

Graphene layers were passivated with SiO_2 by using PED technique in order to suppress the interactions of sample with atmospheric gases. IV measurements were conducted for both CVDG and EG after the encapsulation process and the obtained results are compared in Figure 4.10 (b) and (c).

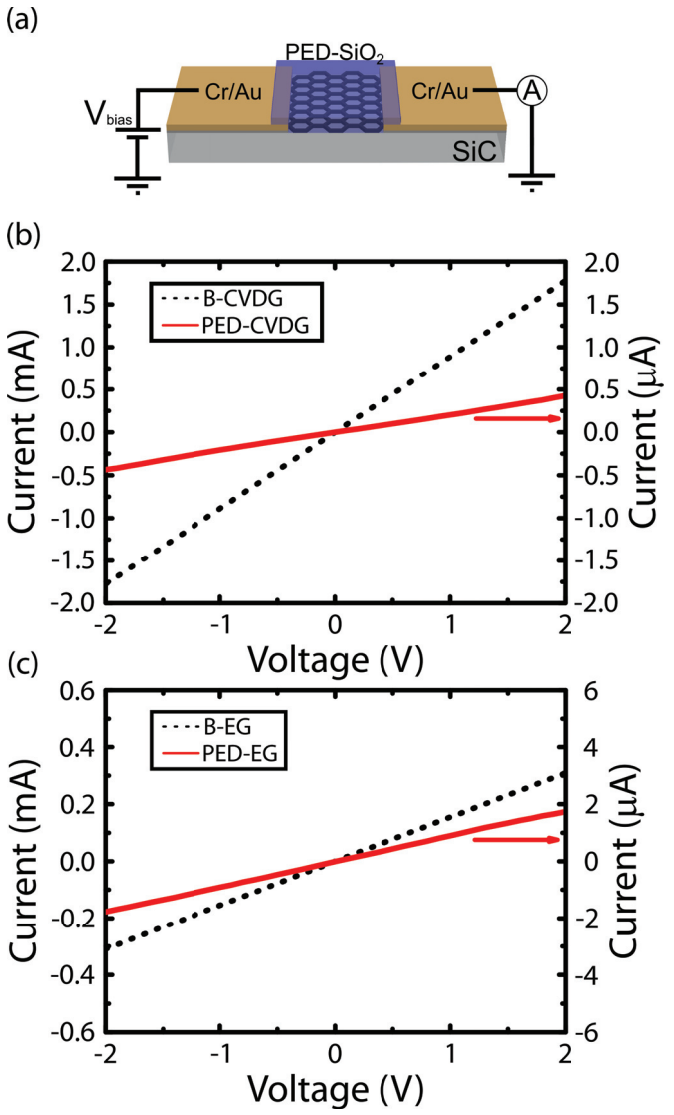

Figure 4.10. (a) Device schematics after PED encapsulation. The IV characteristics of (b) CVDG and (c) EG before and after PED encapsulation.

The initial resistance of bare CVDG was measured as $1.1\ k\Omega$ and after the PED encapsulation its resistance was found to be increased to $4.7\ M\Omega$ (Figure 4.10 (b)).

As seen in Figure 4.10 (c), the initial resistance of bare EG is $6.5\ k\Omega$, while the PED-EG has the resistance of $1.2\ M\Omega$. These increments of the sample resistances can be attributed to the passivation of the dangling bonds responsible from the electrical conductivity in graphene layer.

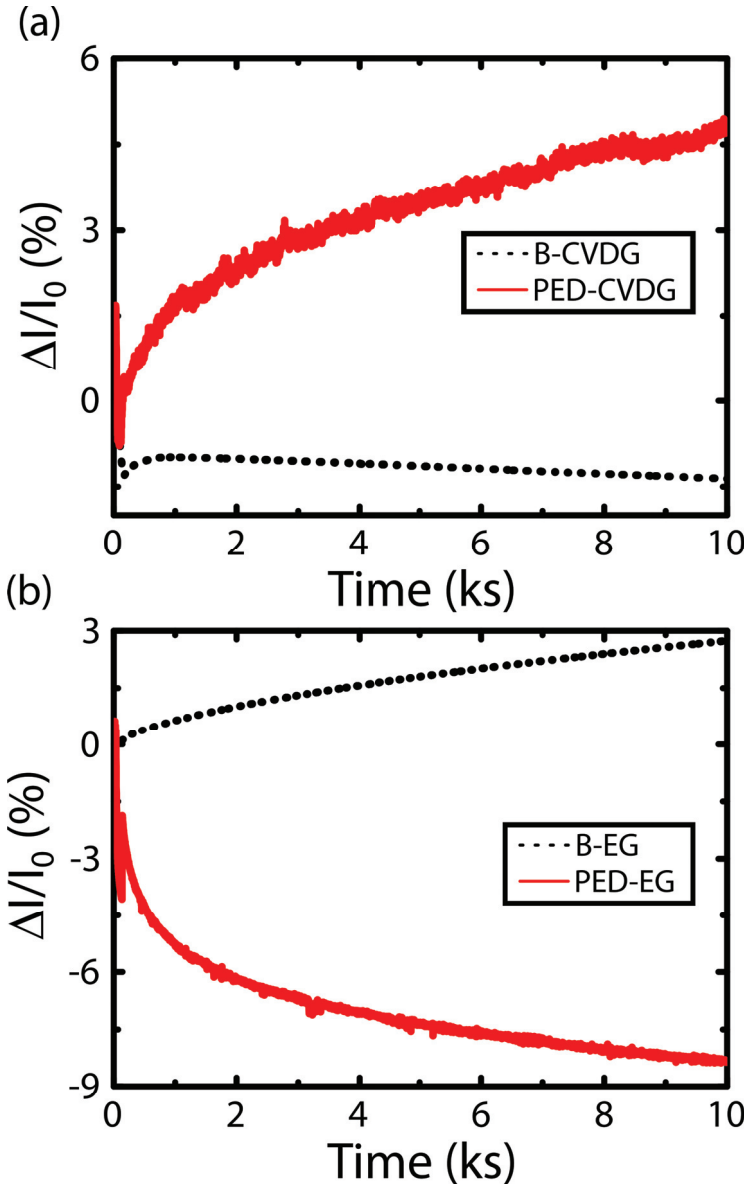

Figure 4.11. The time dependent resistance variations of (a) CVDG and (b) EG under vacuum before and after PED encapsulation.

For the physisorbed adsorbate contribution of conductivity, vacuum measurements are repeated after encapsulation (Figure 4.11). A drastic resistance alteration was observed after PED encapsulation for both types of graphene.

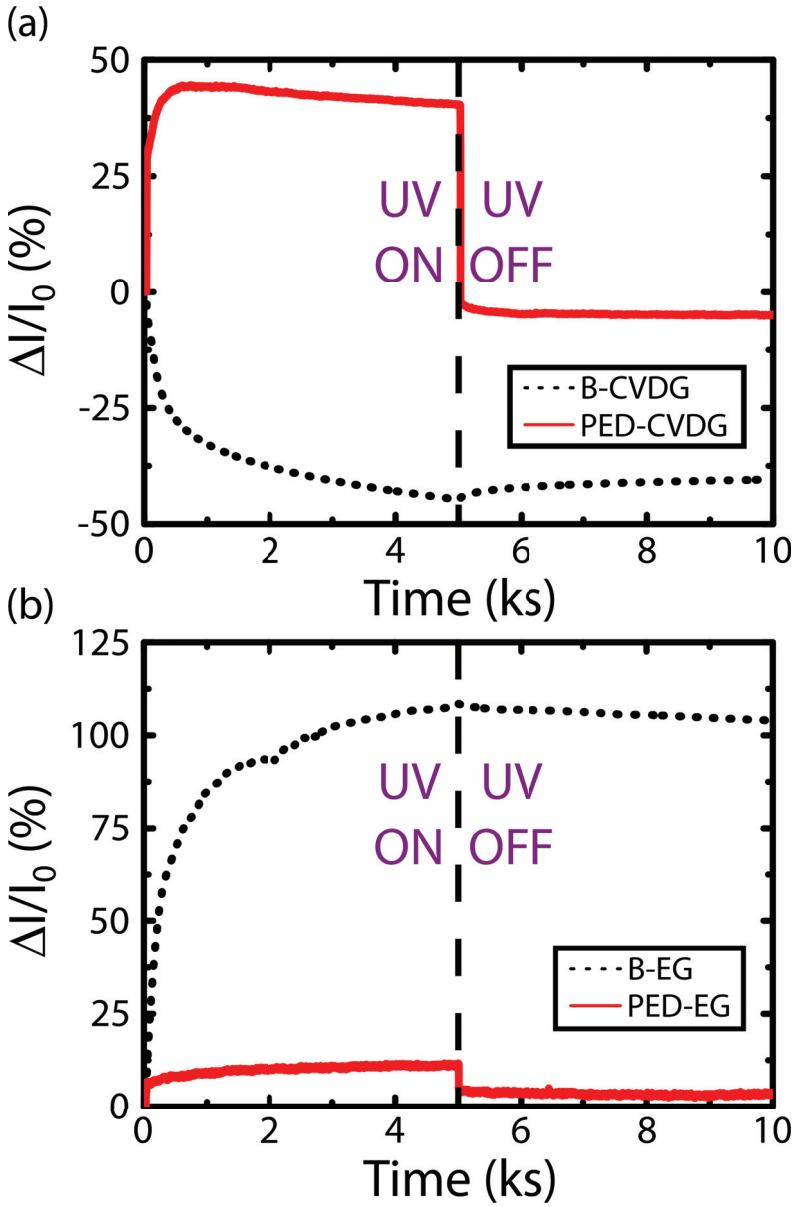

Figure 4.12. The $5\ ks$ one cycle transient photocurrent spectrum of (a) CVDG and (b) EG before and after PED encapsulation.

The UV light leads to a rapid increase in the measured currents of the PED encapsulated ones, unlike the bare ones. When the UV light is turned off, the current drops sharply down to its initial value within only one second. As seen in Figure 4.12, such a fast on/off transition in the currents of encapsulated samples is dominated by the photogenerated charge carriers created in the depletion region of SiC substrate underneath and not by desorption/adsorption of the adsorbates on the graphene layer.

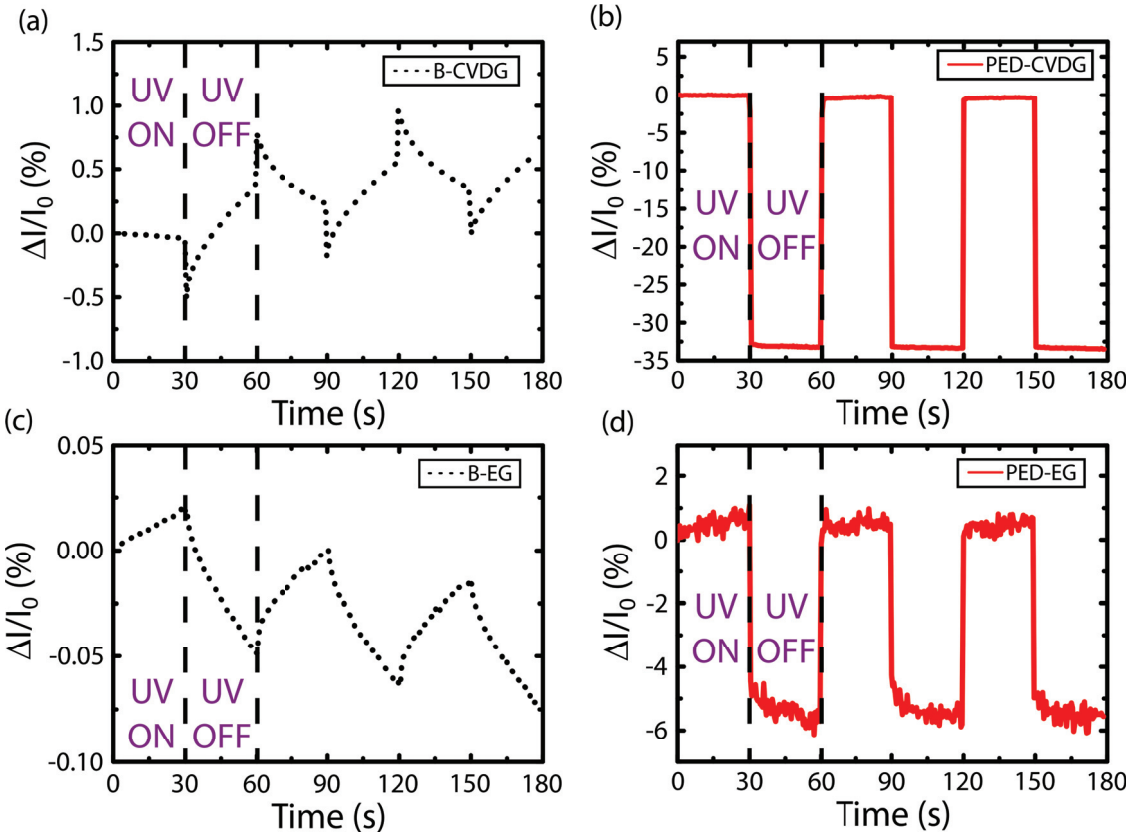

Figure 4.13. The 30 s three cycle transient photocurrent spectrum of (a) CVDG and (b) EG before and after PED encapsulation.

The results of TPS measurements acquired before and after the PED encapsulation process are shown in Figure 4.13. The spectra that belong to bare and PED encapsulated CVDG are compared in Figure 4.13 (a) and (b), respectively. Unlike B-CVDG, the TPS plot of the PED-CVDG one exhibits uniform and stable profiles, revealing that the sample had an excellent photocurrent reversibility and a fast response speed (Figure 4.13 (b)). In addition, the magnitude of the current change in B-CVDG sample was found to be increased from 1 % to 34 % when it is encapsulated with PED. As displayed in Figure 4.13 (d), the current of the sample could be reversibly modulated by UV illumination, indicating good reproducibility and stability of the PED-EG. The small amplitude variations seen in the measured current is attributed to the hole traps at the EG/SiC interface. It is obvious that we achieved a complete passivation with the PED encapsulation.

4.3. The Mechanism Behind the Adsorption/Desorption Process

The illustrations in Figure 4.14 display the adsorption/desorption induced charge carrier dynamics for CVDG and EG, and give an insight into the experimental results presented in Figure 4.13. For the samples with bare graphene layer, the conductivity is modified by the adsorption/desorption of adsorbates and photogenerated charge carriers from underlying SiC substrate together. The experimentally obtained results manifest that the conductivity of bare CVDG (σ_{CVDG}) changes as in the form of $\Delta\sigma_{CVDG} \propto \sigma_{ph} - \sigma_{ad}(t)$ (compare Figure 4.13 (a)) whereas the change in the conductivity of bare EG (σ_{EG}) takes the form of $\Delta\sigma_{EG} \propto \sigma_{ph} + \sigma_{ad}(t)$ (compare Figure 4.13 (c)). Here, σ_{ph} is the contribution of photogenerated charge carriers and σ_{ad} is the contribution of the adsorbates to the graphenes conductivity. As can be understood from the TPS measurements shown in Figure 4.13, $\sigma_{ad}(t)$ is indeed a time dependent exponentially varying function. The adsorbate layer on graphene absorbs most of the UV photons impinging on the sample surface for desorption process and thus strongly hinders the formation of photo-generated charge carriers in the depletion layer of SiC underneath. When the UV light is off, the change in the conductivity becomes $\Delta\sigma_{CVDG} \propto \sigma_{ad}(t) - \sigma_{ph}$ for bare CVDG and $\Delta\sigma_{EG} \propto -\sigma_{ph} - \sigma_{ad}(t)$ for bare EG due to the adsorption of the adsorbates with low partial pressure in the corresponding vacuum level. However, when the samples are encapsulated, the contribution of the adsorbates to the graphenes conductivity is suppressed and therefore the UV light produces only the photo-generated carriers in the depletion layer of SiC. These photo-generated charge carriers modify the conductivity of the graphene layers via charge transfer doping process. Because of the fact that the conductivity variation in the encapsulated samples takes a time independent form of $\sigma \propto \sigma_{ph}$ as schematically depicted in Figure 4.14 (b) and (d).

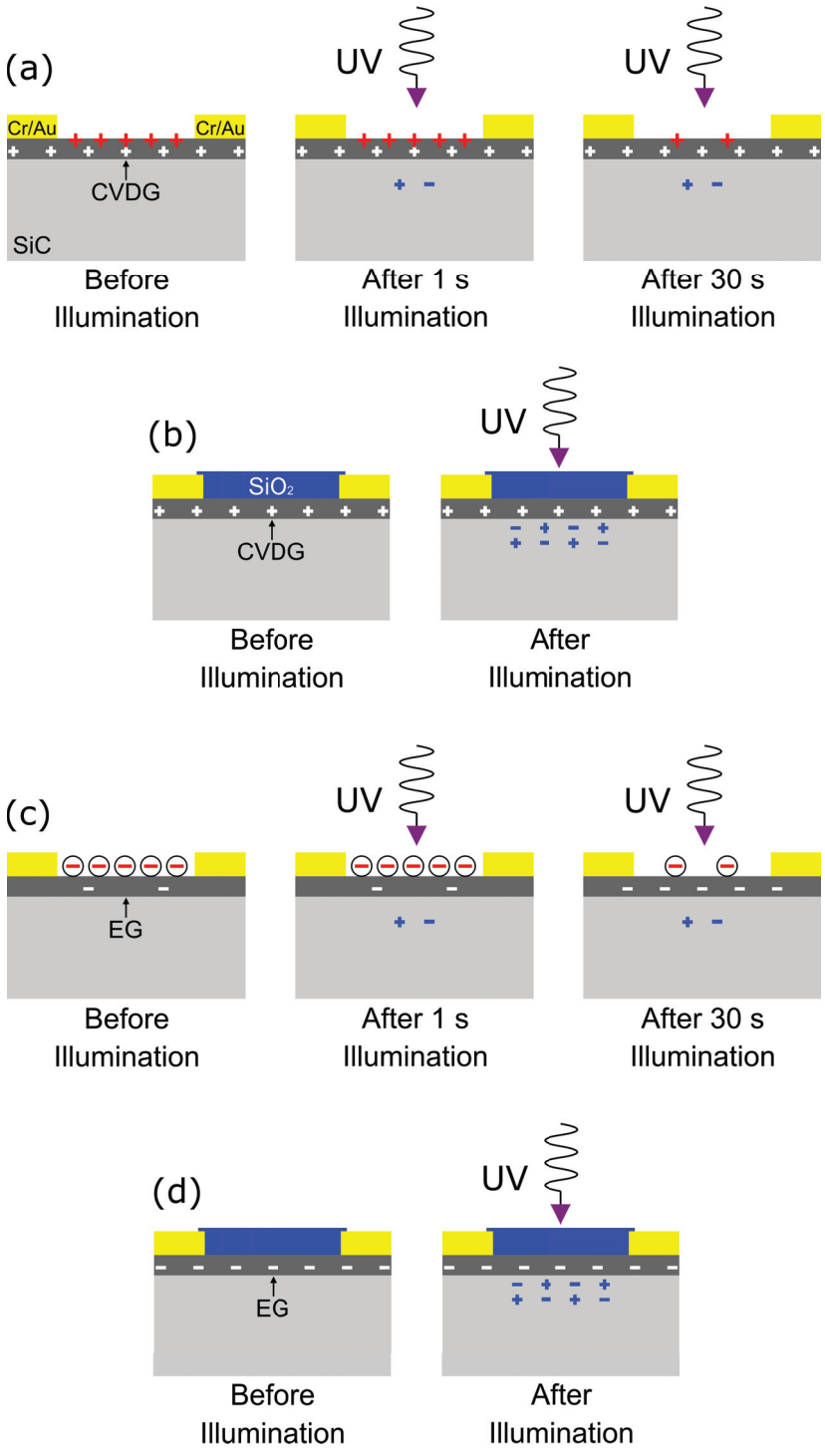

Figure 4.14. The schematic side view of adsorption/desorption driven charge carrier dynamics for (a) B-CVDG, (b) PED-CVDG, (c) B-EG and (d) PED-EG. White colored charges represent the intrinsic charge carriers in graphene layers, red colored charges depict the injected (for CVDG) or trapped (for EG) charge carriers by the adsorbates and the blue colored charges are the photo-generated charge carriers formed at the depletion region of SiC substrate underneath the graphene layers (the sketch is not scaled).

4.4. Thermistor Behavior as a Result of Surface Passivation

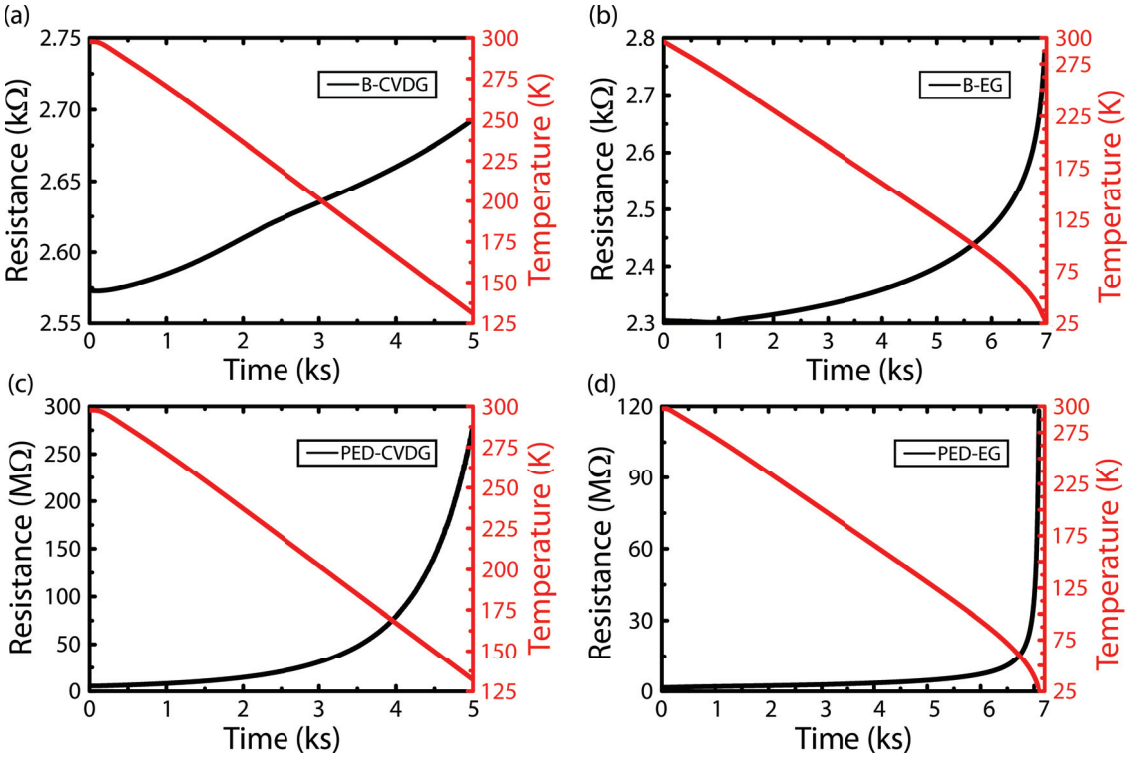

Figure 4.15. The temperature dependent resistance measurements of (a) B-CVDG, (b) B-EG, (c) PED-CVDG and (d) PED-EG samples.

When the two system are thermally contacted, the temperature gradient will result with a thermal equilibrium as the zeroth law of thermodynamics. In our closed cycle cryostat, the air between the cold finger and the shield of the cryostat provides the thermal equilibrium. When cryostat is vacuumed, the thermal equilibrium between the shield and cold finger is broken. Therefore, cold finger may get colder or warmer depends on initial conditions which is the surrounding ambient. The unexpected behaviors in vacuum measurements after PED encapsulation lead to think about on the question: "Do the samples become more sensitive to temperature or not after encapsulation?". A calibrated thermocouple was connected to the cold finger to detect the temperature, while the resistance of the graphene samples were measured. As seen in Figure 4.15, PED encapsulated samples are observed extremely sensitive to temperature alterations in comparison to bare samples.

CHAPTER 5

CONCLUSION

In summary, we have investigated the impact of atmospheric adsorbates on the electrical stability of graphene layers with two different charge carrier types. The Transient Photocurrent Spectroscopy measurements of ZnO and the conductivity alterations of graphene is given a sight to examine the Transient Photocurrent Spectrums of graphene layers for the first time in literature. The measurements proved that the adsorption/desorption of adsorbates indeed modifies the conductivity of graphene, but in a distinct manner depending on whether it is n-type (as in epitaxial graphene) or p-type doped (as in CVD graphene) and act as the main source for time dependent electrical instability. Adsorbate induced variations seen in the conductivity of n-type graphene was found to be consistent with the conductivity instabilities in n-type metal-oxide semiconductors like ZnO thin films subject to atmospheric environment. For p-type materials with high surface-to-volume ratio, we expect also adsorbate induced conductivity instabilities but in the same manner as we experimentally observed for CVD graphene in this study. Graphene layers are attempted to passivate by thermal evaporated SiO_2 thin films. The supression of adsorbate interaction was found to be insufficient. The encapsulation of graphene with PED grown SiO_2 was found to successfully hinder the adsorption/desorption of atmospheric adsorbates and therefore maintains the electrical stability of graphene independent of its charge carrier type. Our experimentally obtained results can be used to interpret the adsorbate induced conductivity variations that may occur in other materials like 2D systems with an inherently high surface-to-volume ratio.

REFERENCES

An, Y., A. Behnam, E. Pop, and A. Ural (2013). Metal-semiconductor-metal photodetectors based on graphene/p-type silicon schottky junctions. *Applied Physics Letters 102*(1), 013110.

Aydin, H., C. Bacaksiz, N. Yagmurcukardes, C. Karakaya, O. Mermer, M. Can, R. Senger, H. Sahin, and Y. Selamet (2018). Experimental and computational investigation of graphene/sams/n-si schottky diodes. *Applied Surface Science 428*, 1010–1017.

Bolotin, K. I., K. J. Sikes, Z. D. Jiang, M. Klima, G. Fudenberg, J. Hone, P. H. Kim, and H. L. Stormer (2008). Ultrahigh electron mobility in suspended graphene. *Solid State Communications 146*(9), 351–355.

Bonaccorso, F., Z. Sun, T. A. Hasan, and A. C. Ferrari (2010). Graphene photonics and optoelectronics. *Nature photonics 4*(9), 611–622.

Chen, C.-C., M. Aykol, C.-C. Chang, A. Levi, and S. B. Cronin (2011). Graphene-silicon schottky diodes. *Nano letters 11*(5), 1863–1867.

Cooper, D. R., B. DAnjou, N. Ghattamaneni, B. Harack, M. Hilke, A. Horth, N. Majlis, M. Massicotte, L. Vandsburger, and E. Whiteway (2012). Experimental review of graphene. *ISRN Condensed Matter Physics 2012*.

Danielson, P. (1987, April 28). Desorption of water molecules in a vacuum system using ultraviolet radiation. US Patent 4,660,297.

Dash, G. N., S. R. Pattanaik, and S. Behera (2014). Graphene for electron devices: the panorama of a decade. *IEEE Journal of the Electron Devices Society 2*(5), 77–104.

Eriksson, J., R. Pearce, T. Iakimov, C. Virojanadara, D. Gogova, M. Andersson, M. Syväjärvi, A. Lloyd Spetz, and R. Yakimova (2012). The influence of substrate morphology on thickness uniformity and unintentional doping of epitaxial graphene on sic. *Applied Physics Letters 100*(24), 241607.

Geim, A., K. Novoselov, and S. Konstantin (2007). The rise of graphene. *Nature materials 6*(3), 183–191.

Grill, L. (2016). Supramolecular chemistry at surfaces. by david b. amabilino.

Gross, A. (2014). *Theoretical surface science*, Volume 1. Springer.

Jariwala, D., V. K. Sangwan, D. J. Late, J. E. Johns, V. P. Dravid, T. J. Marks, L. J. Lauhon, and M. C. Hersam (2013). Band-like transport in high mobility unencapsulated single-layer mos2 transistors. *Applied Physics Letters 102*(17), 173107.

Kopylov, S., A. Tzalenchuk, S. Kubatkin, and V. I. Falko (2010). Charge transfer between epitaxial graphene and silicon carbide. *Applied Physics Letters 97*(11), 112109.

Kus, E., D. Özkendir, V. Fırat, C. Çelebi, et al. (2015). Epitaxial graphene contact elec-

trode for silicon carbide based ultraviolet photodetector. *Journal of Physics D: Applied Physics 48*(9), 095104.

Li, Q. H., T. Gao, Y. G. Wang, and T. H. Wang (2005). Adsorption and desorption of oxygen probed from zno nanowire films by photocurrent measurements. *Applied Physics Letters 86*(12), 123117.

Li, X., M. Zhu, M. Du, Z. Lv, L. Zhang, Y. Li, Y. Yang, T. Yang, X. Li, K. Wang, et al. (2016). High detectivity graphene-silicon heterojunction photodetector. *Small 12*(5), 595–601.

Li, Y., F. Della Valle, M. Simonnet, I. Yamada, and J.-J. Delaunay (2009). Competitive surface effects of oxygen and water on uv photoresponse of zno nanowires. *Applied Physics Letters 94*(2), 023110.

Lin, Z., X. Ye, J. Han, Q. Chen, P. Fan, H. Zhang, D. Xie, H. Zhu, and M. Zhong (2015). Precise control of the number of layers of graphene by picosecond laser thinning. *Scientific reports 5*, 11662.

Nomani, M. W., A. Singh, V. Shields, M. Spencer, G. Tompa, N. Sbrockey, and G. Koley (2011). Work function and conductivity changes due to molecular adsorption in epitaxial graphene on 6h-sic. In *Nanotechnology (IEEE-NANO), 2011 11th IEEE Conference on*, pp. 1317–1321. IEEE.

Peres, N. M. R. (2010). Colloquium: The transport properties of graphene: An introduction. *Reviews of Modern Physics 82*(3), 2673.

Pirkle, A., J. Chan, A. Venugopal, D. Hinojos, C. Magnuson, S. McDonnell, L. Colombo, E. Vogel, R. Ruoff, and R. Wallace (2011). The effect of chemical residues on the physical and electrical properties of chemical vapor deposited graphene transferred to sio2. *Applied Physics Letters 99*(12), 122108.

Ryu, S., L. Liu, S. Berciaud, Y.-J. Yu, H. Liu, P. Kim, G. W. Flynn, and L. E. Brus (2010). Atmospheric oxygen binding and hole doping in deformed graphene on a sio2 substrate. *Nano letters 10*(12), 4944–4951.

Schedin, F., A. Geim, S. Morozov, E. Hill, P. Blake, M. Katsnelson, and K. Novoselov (2007). Detection of individual gas molecules adsorbed on graphene. *Nature materials 6*(9), 652–655.

Shivaraman, S., M. Chandrashekhar, J. J. Boeckl, and M. G. Spencer (2009). Thickness estimation of epitaxial graphene on sic using attenuation of substrate raman intensity. *Journal of electronic materials 38*(6), 725–730.

Sidorov, A. N., K. Gaskill, M. Buongiorno Nardelli, J. L. Tedesco, R. L. Myers-Ward, C. R. Eddy Jr, T. Jayasekera, K. W. Kim, R. Jayasingha, A. Sherehiy, et al. (2012). Charge transfer equilibria in ambient-exposed epitaxial graphene on (000 1$^-$) 6 h-sic. *Journal of Applied Physics 111*(11), 113706.

Suk, J. W., W. H. Lee, J. Lee, H. Chou, R. D. Piner, Y. Hao, D. Akinwande, and R. S. Ruoff (2013). Enhancement of the electrical properties of graphene grown by chemical vapor deposition via controlling the effects of polymer residue. *Nano letters 13*(4), 1462–1467.

Tongay, S., M. Lemaitre, T. Schumann, K. Berke, B. R. Appleton, B. Gila, and A. F. Hebard (2011). Graphene/gan schottky diodes: Stability at elevated temperatures. *Applied Physics Letters 99*(10), 102102.

Tongay, S., T. Schumann, and A. Hebard (2009). Graphite based schottky diodes formed on si, gaas, and 4h-sic substrates. *Applied Physics Letters 95*(22), 222103.

Tricot, S., C. Boulmer-Leborgne, M. Nistor, E. Millon, and J. Perrière (2008). Dynamics of a pulsed-electron beam induced plasma: application to the growth of zinc oxide thin films. *Journal of Physics D: Applied Physics 41*(17), 175205.

Xia, Y., H. Zhao, S. Liu, and T. Zhang (2014). The humidity-sensitive property of mcm-48 self-assembly fiber prepared via electrospinning. *RSC Advances 4*(6), 2807–2812.

Yang, Y. and R. Murali (2011). Binding mechanisms of molecular oxygen and moisture to graphene. *Applied Physics Letters 98*(9), 093116.